Supplemental Information: From Molecular to Macroscopic: Predicting Liquid-Liquid Phase Equilibria and Small-Angle Scattering of Mixtures of Organic Liquids from Atomistic Simulation using Kirkwood-Buff Theory

Allison A. Peroutka,*,† G. Brian Stephenson,*,‡ and Michael J. Servis*,†

†*Chemical Sciences and Engineering Division, Argonne National Laboratory, 9700 S Cass Ave, Lemont, IL 60439*

‡*Materials Science Division, Argonne National Laboratory, Lemont, IL 60439, USA*

E-mail: aperoutka@anl.gov; gbs@anl.gov; mservis@anl.gov

System Compositions

The following tables contain system composition information for the six systems considered in this study along with pure component information, where N is the number of molecules, x is the mole fraction, and ϕ is the volume fraction.

Table S1: Number of molecules used in pure component simulations.

Component	N
DOHE	1008
DBP	1557
n-hexane	4577
n-heptane	4087
n-octane	3706
n-decane	3090
n-dodecane	2652

Table S2: System compositions for DBP in n-dodecane.

Sample No.	N_{DBP}	$N_{n-dodecane}$	x_{DBP}	$x_{n-dodecane}$	ϕ_{DBP}	$\phi_{n-dodecane}$
1	180	2386	0.070	0.930	0.098	0.902
2	361	2121	0.145	0.855	0.196	0.804
3	541	1856	0.226	0.774	0.295	0.705
4	721	1591	0.312	0.688	0.394	0.606
5	902	1326	0.405	0.595	0.494	0.506
6	1082	1061	0.505	0.495	0.594	0.406
7	1263	795	0.614	0.386	0.695	0.305
8	1443	530	0.731	0.269	0.796	0.204
9	1623	265	0.860	0.140	0.898	0.102

Table S3: System compositions for DBP in *n*-decane.

Sample No.	N_{DBP}	$N_{n-decane}$	x_{DBP}	$x_{n-decane}$	ϕ_{DBP}	$\phi_{n-decane}$
1	156	2781	0.053	0.947	0.085	0.915
2	311	2472	0.112	0.888	0.173	0.827
3	467	2163	0.178	0.822	0.264	0.736
4	623	1854	0.252	0.748	0.358	0.642
5	779	1545	0.335	0.665	0.456	0.544
6	934	1236	0.430	0.570	0.557	0.443
7	1090	927	0.540	0.460	0.662	0.338
8	1246	618	0.668	0.332	0.770	0.230
9	1402	309	0.819	0.181	0.883	0.117

Table S4: System compositions for DBP in *n*-octane.

Sample No.	N_{DBP}	$N_{n-octane}$	x_{DBP}	$x_{n-octane}$	ϕ_{DBP}	$\phi_{n-octane}$
1	156	3335	0.045	0.955	0.084	0.916
2	311	2965	0.095	0.905	0.171	0.829
3	467	2594	0.153	0.847	0.261	0.739
4	623	2224	0.219	0.781	0.355	0.645
5	779	1853	0.296	0.704	0.452	0.548
6	934	1482	0.387	0.613	0.553	0.447
7	1090	1112	0.495	0.505	0.658	0.342
8	1246	741	0.627	0.373	0.768	0.232
9	1402	371	0.791	0.209	0.881	0.119

Table S5: System compositions for DBP in *n*-hexane.

Sample No.	N_{DBP}	$N_{n-hexane}$	x_{DBP}	$x_{n-hexane}$	ϕ_{DBP}	$\phi_{n-hexane}$
1	156	4119	0.036	0.964	0.082	0.918
2	311	3662	0.078	0.922	0.167	0.833
3	467	3204	0.127	0.873	0.256	0.744
4	623	2746	0.185	0.815	0.349	0.651
5	779	2288	0.254	0.746	0.446	0.554
6	934	1831	0.338	0.662	0.547	0.453
7	1090	1373	0.443	0.557	0.653	0.347
8	1246	915	0.577	0.423	0.763	0.237
9	1402	458	0.754	0.246	0.879	0.121

Table S6: System compositions for DOHE in n-dodecane.

Sample No.	N_{DOHE}	$N_{n-dodecane}$	x_{DOHE}	$x_{n-dodecane}$	ϕ_{DOHE}	$\phi_{n-dodecane}$
1	101	2386	0.041	0.959	0.087	0.913
2	202	2121	0.087	0.913	0.177	0.823
3	302	1856	0.140	0.860	0.268	0.732
4	403	1591	0.202	0.798	0.363	0.637
5	504	1326	0.275	0.725	0.461	0.539
6	605	1061	0.363	0.637	0.562	0.438
7	706	795	0.470	0.530	0.667	0.333
8	806	530	0.603	0.397	0.774	0.226
9	907	265	0.774	0.226	0.885	0.115

Table S7: System compositions for DOHE in n-heptane.

Sample No.	N_{DOHE}	$N_{n-heptane}$	x_{DOHE}	$x_{n-heptane}$	ϕ_{DOHE}	$\phi_{n-heptane}$
1	101	3678	0.027	0.973	0.085	0.915
2	202	3269	0.058	0.941	0.173	0.827
3	302	2861	0.095	0.904	0.263	0.737
4	403	2452	0.141	0.858	0.357	0.643
5	504	2043	0.198	0.802	0.454	0.545
6	605	1635	0.270	0.729	0.555	0.444
7	706	1226	0.365	0.634	0.660	0.339
8	806	817	0.497	0.503	0.769	0.230
9	907	409	0.689	0.310	0.882	0.117

Kirkwood-Buff Integral Corrections

Calculation of Kirkwood-Buff Integrals (KBIs) from constant particle simulations, either in the NVT or NpT ensemble, requires two corrections. These involve correcting for 1) divergence of the pair correlation function $g_{ij}(r)$ as $r \to R$ and 2) extrapolation of finite volume KBI to the thermodynamic limit where relationships between KBIs and thermodynamic properties are rigorously defined.

We correct for the divergence of $g_{ij}(r)$ by applying the approach demonstrated by Milzetti et al.,[1] that first corrects the $g_{ij}(r)$ according to Ganguly and van der Vegt,[2] followed by applying a damping function from Krüger et al..[3] These corrections result in the following calculation for KBI,

$$G_{ij}^{R} = \int_0^R 4\pi r^2 \omega(r)(g_{ij}^{Ganguly}(r) - 1)dr, \tag{S1}$$

where $\omega(r)$ is the damping function and $g_{ij}^{Ganguly}(r)$ is the corrected pair correlation function. The first correction adjusts the particle count within the radius r_{max} using,

$$\begin{aligned} g_{ij}^{Ganguly}(r) &= g_{ij}^{NpT}(r)\left[\frac{N_j f(r)}{N_j f(r) - \Delta N_{ij}(r) - \delta_{ij}}\right], \\ f(r) &= 1 - \frac{\frac{4}{3}\pi r^3}{V_{tot}}, \\ \Delta N_{ij}(r) &= \rho_j \int_0^{r_{max}} 4\pi r^2 (g_{ij}^{NpT}(r) - 1)dr. \end{aligned} \tag{S2}$$

Here N_j is the number of molecules of j, δ_{ij} is the Kronecker delta, and r_{max} is 1/2 the box length. However, this first correction fails to ensure convergence. Krüger et al.[3] subsequently introduced a damping function to achieve this,[2–4]

$$\omega(r) = \left[1 - \left(\frac{r}{r_{max}}\right)^3\right]. \tag{S3}$$

This damping function primarily impacts the value of the tail.

After applying convergence corrections, we followed the approach of Simon et al.[5] to

extrapolate finite-size KBIs to the thermodynamic limit. In this method, thermodynamic limit KBI G_{ij}^{∞} is related to the running KBI G_{ij}^{R} at finite cutoff R by

$$R\,G_{ij}^{R} = R\,G_{ij}^{\infty} + F_{ij}^{\infty}, \tag{S4}$$

where F_{ij}^{∞} is a finite size surface correction. To estimate G_{ij}^{∞}, we examine the dependence of $R\,G_{ij}^{R}$ on R as $R \to r_{max}$, i.e., the largest accessible sampling volumes relative to the box size. According to Eqn S4, G_{ij}^{∞} is given by the slope of $R\,G_{ij}^{R}$ vs. R over a region of R near r_{max}.

The results of the corrections are shown in Figures S1 - S18. Each row of three panels shows results for one sample composition of a given system. The left panel contains the three pair correlation functions (extractant-extractant, extractant-solvent, and solvent-solvent). To obtain these, we use the atom position best representing the center of mass for each molecule. These were calculated from from 200-1100 ns and 200-600 ns for DOHE and DBP systems, respectively. Colors correspond to each molecule pair, labeled in the legend on the left panel. In the center panel, we show the convergence-corrected running KBI, G_{ij}^{R}, for each molecule pair. The right panel shows extrapolation of the KBI to the thermodynamic limit at large R, with the dashed black lines representing the linear regression (over the last 1 nm) of $R\,G_{ij}^{R}$ vs. R, from which the thermodynamic limit KBI's are determined.

To obtain error estimates on the corrected KBI values, the simulations were split in time, using three 300 ns blocks and four 100 ns blocks for DOHE and DBP systems, respectively. In the RDF calculations, the atom representing the molecular center was used; this corresponds to the carbon atom between both amide groups for the malonamides and the approximate center carbon for the alkanes. The full analysis to obtain the corrected KBI values was performed on the data from each of these blocks, and the variation in these values was used to estimate the standard deviation of the corrected KBI values from the full simulations.

DBP/*n*-dodecane

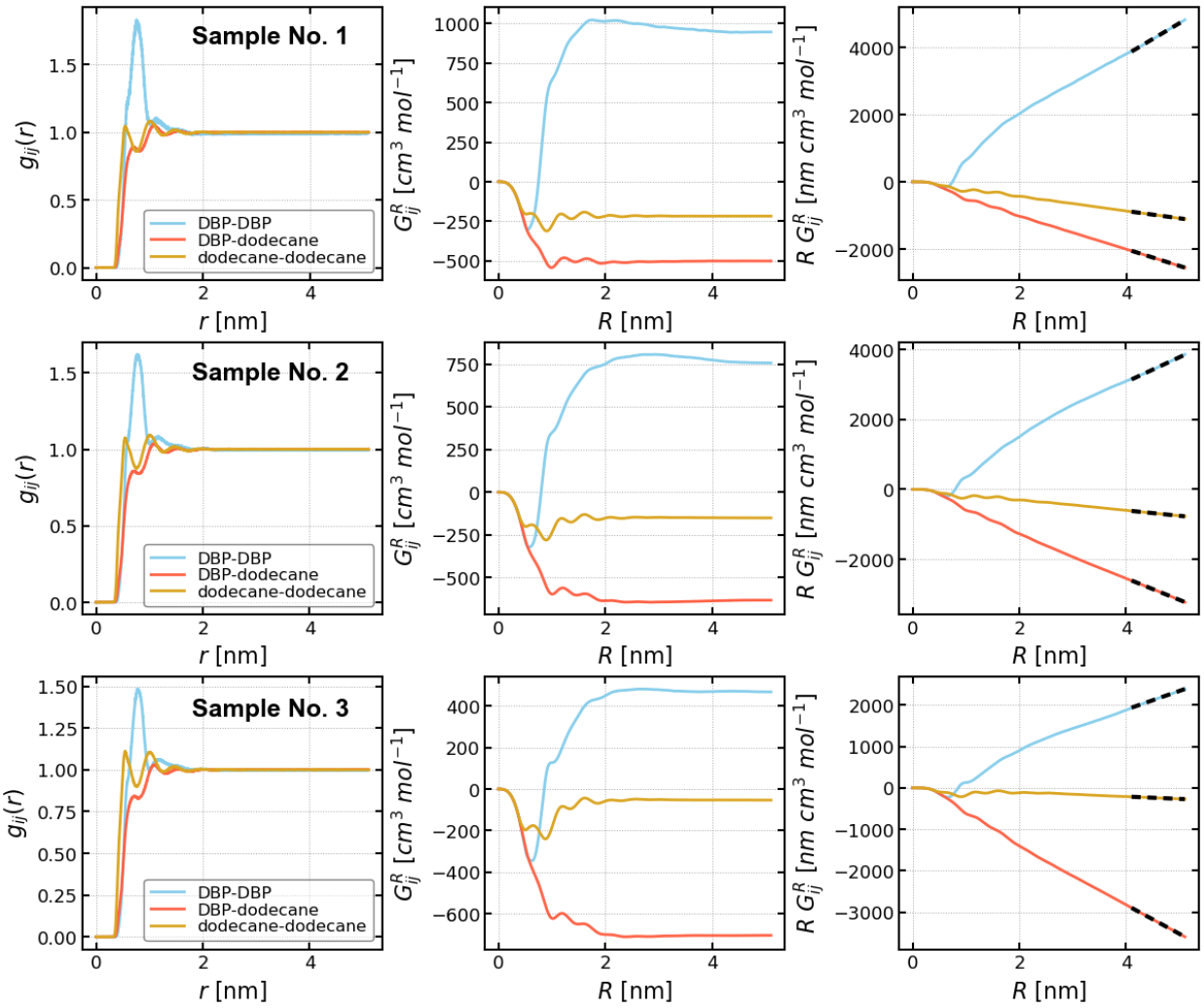

Figure S1: RDF and KBI corrections for DBP/*n*-dodecane system, sample no. 1-3.

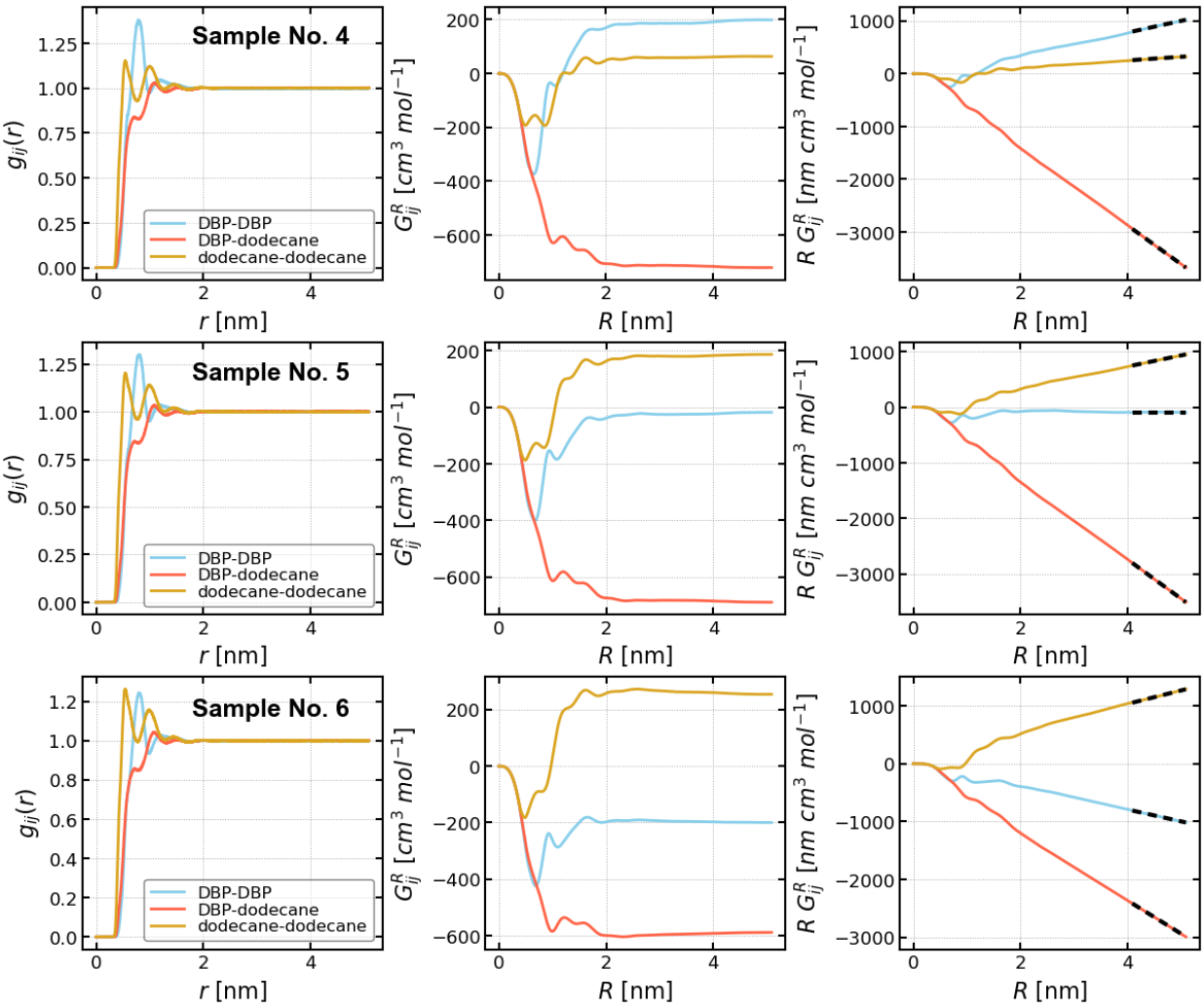

Figure S2: RDF and KBI corrections for DBP/n-dodecane system, sample no. 4-6.

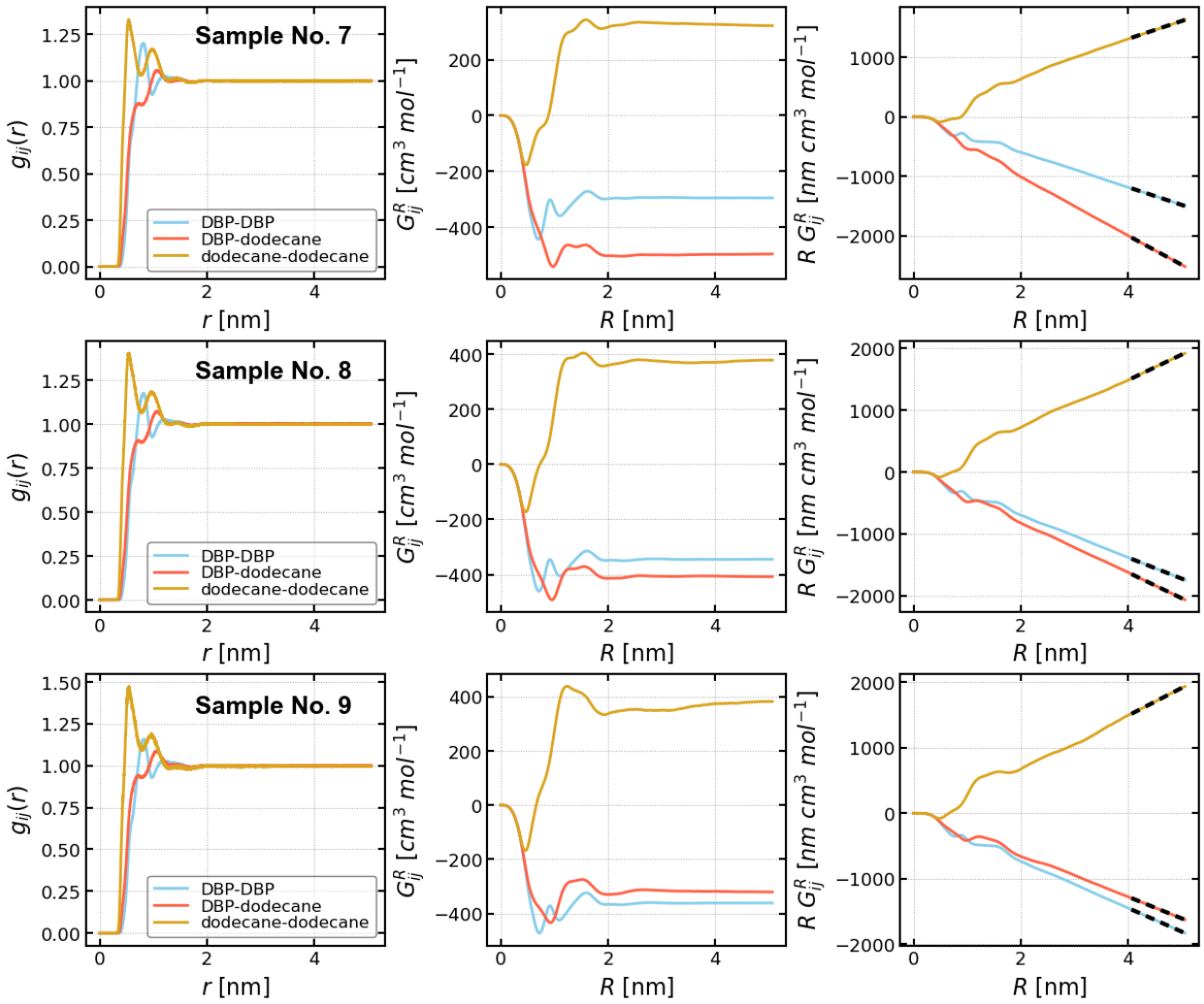

Figure S3: RDF and KBI corrections for DBP/n-dodecane system, sample no. 7-9.

DBP/*n*-decane

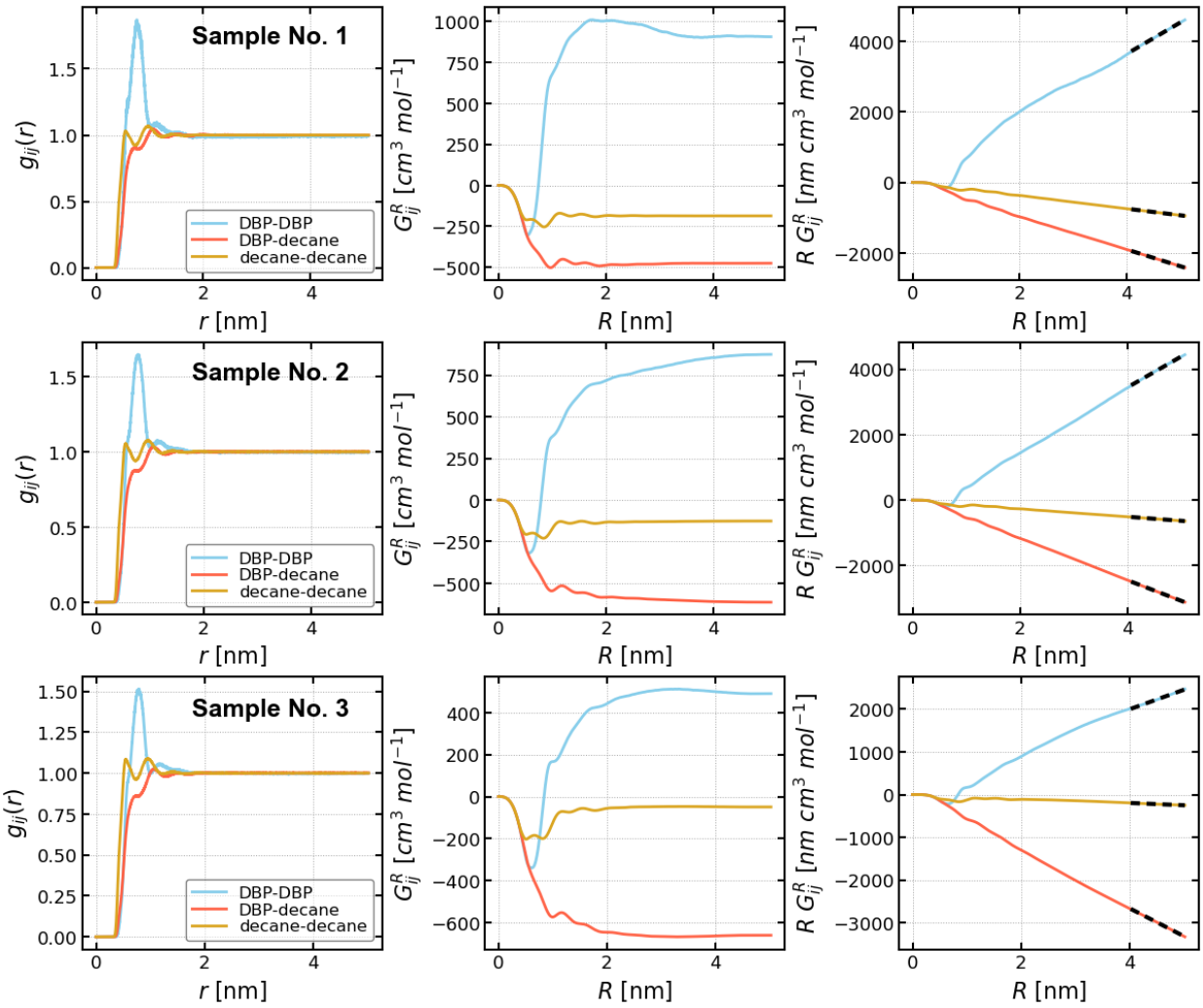

Figure S4: RDF and KBI corrections for DBP/*n*-decane system, sample no. 1-3.

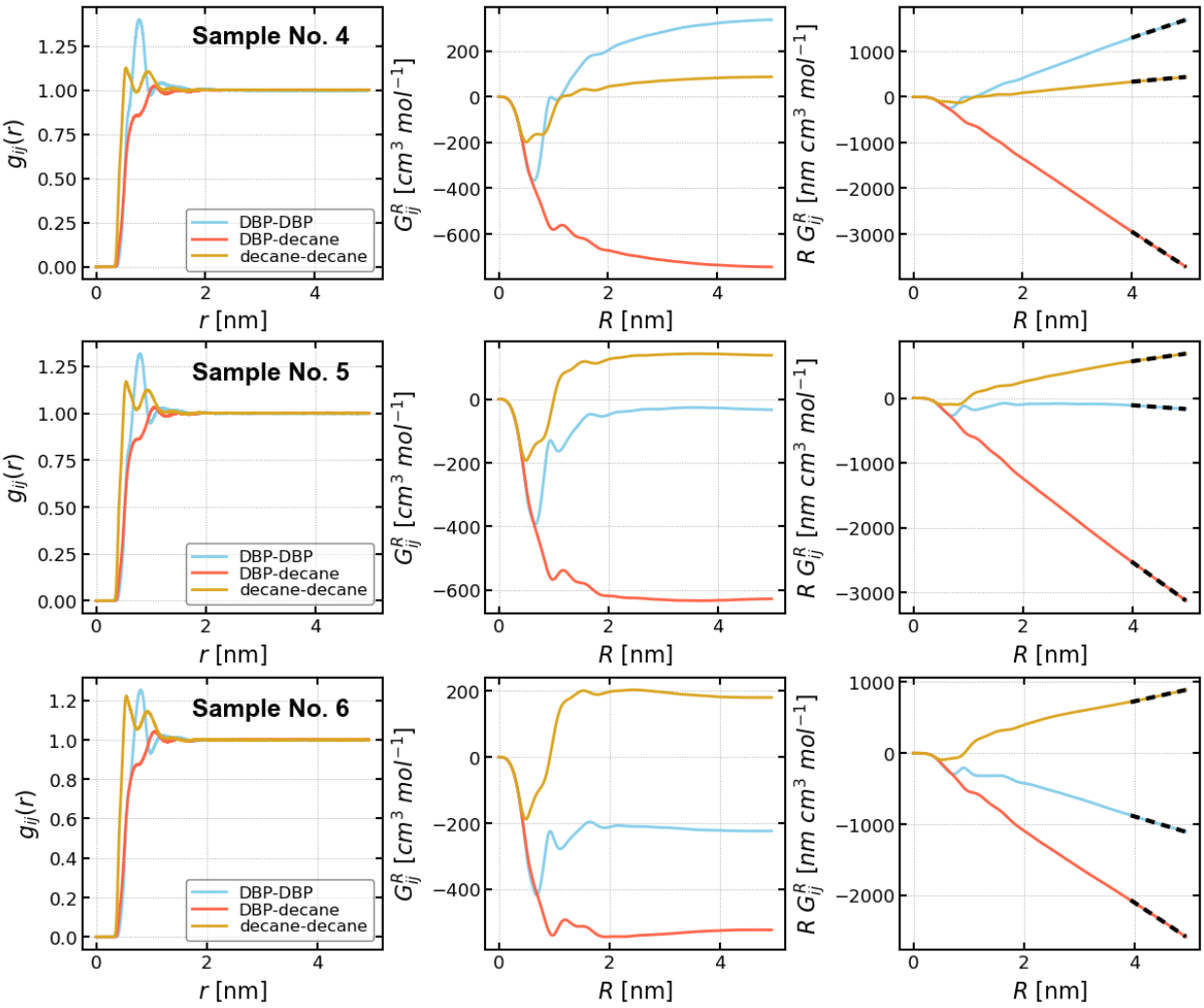

Figure S5: RDF and KBI corrections for DBP/n-decane system, sample no. 4-6.

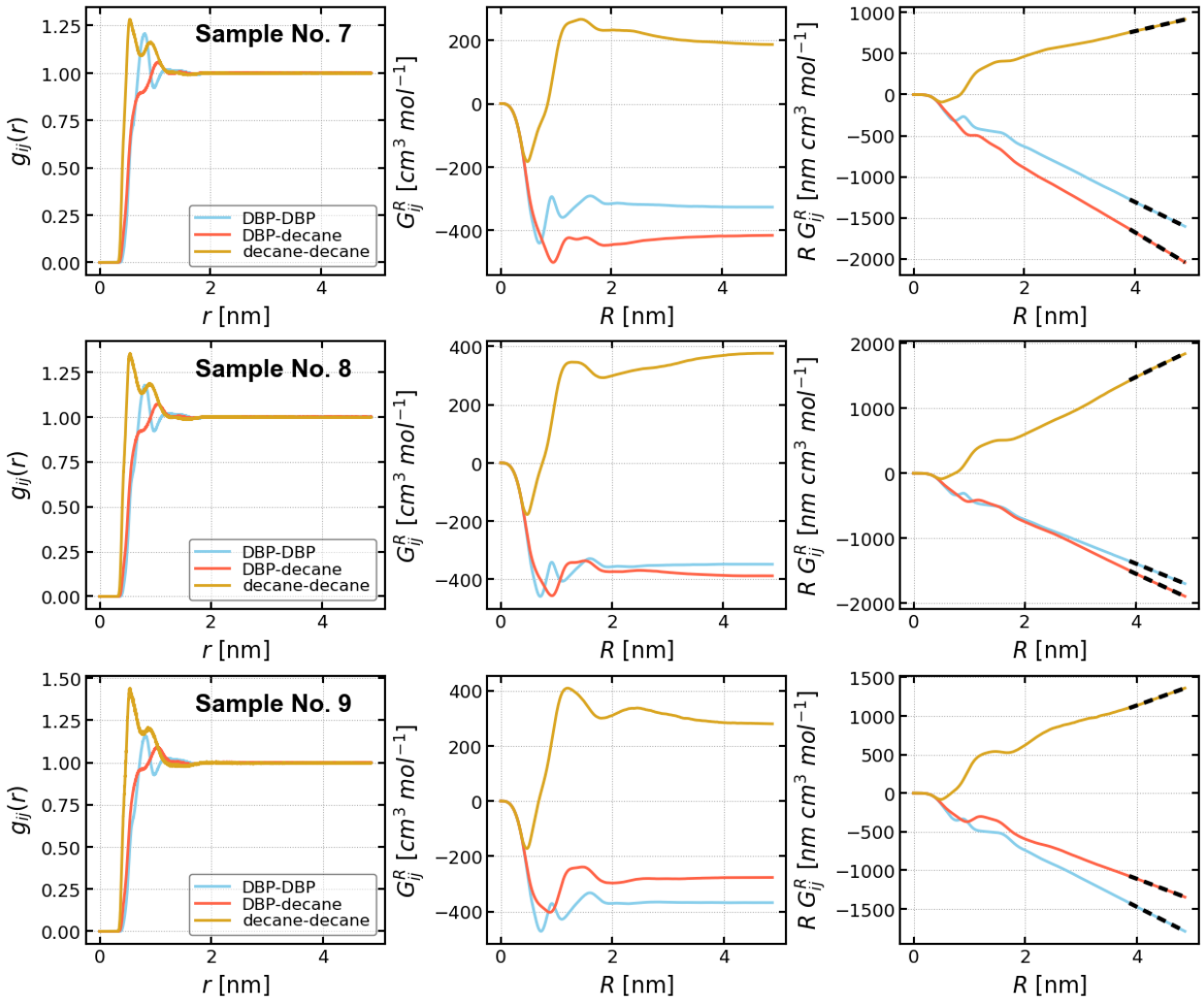

Figure S6: RDF and KBI corrections for DBP/n-decane system, sample no. 7-9.

DBP/*n*-octane

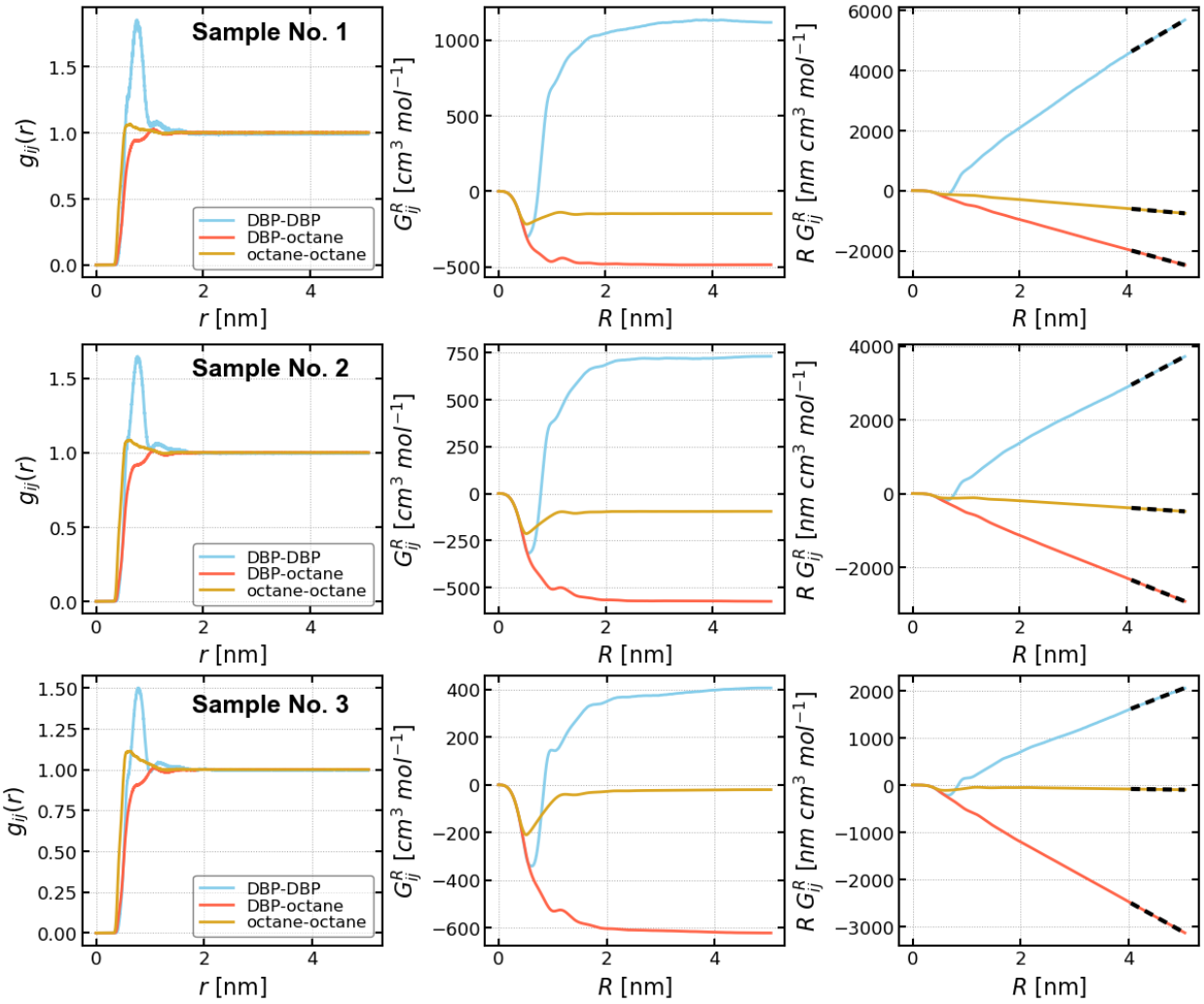

Figure S7: RDF and KBI corrections for DBP/*n*-octane system, sample no. 1-3.

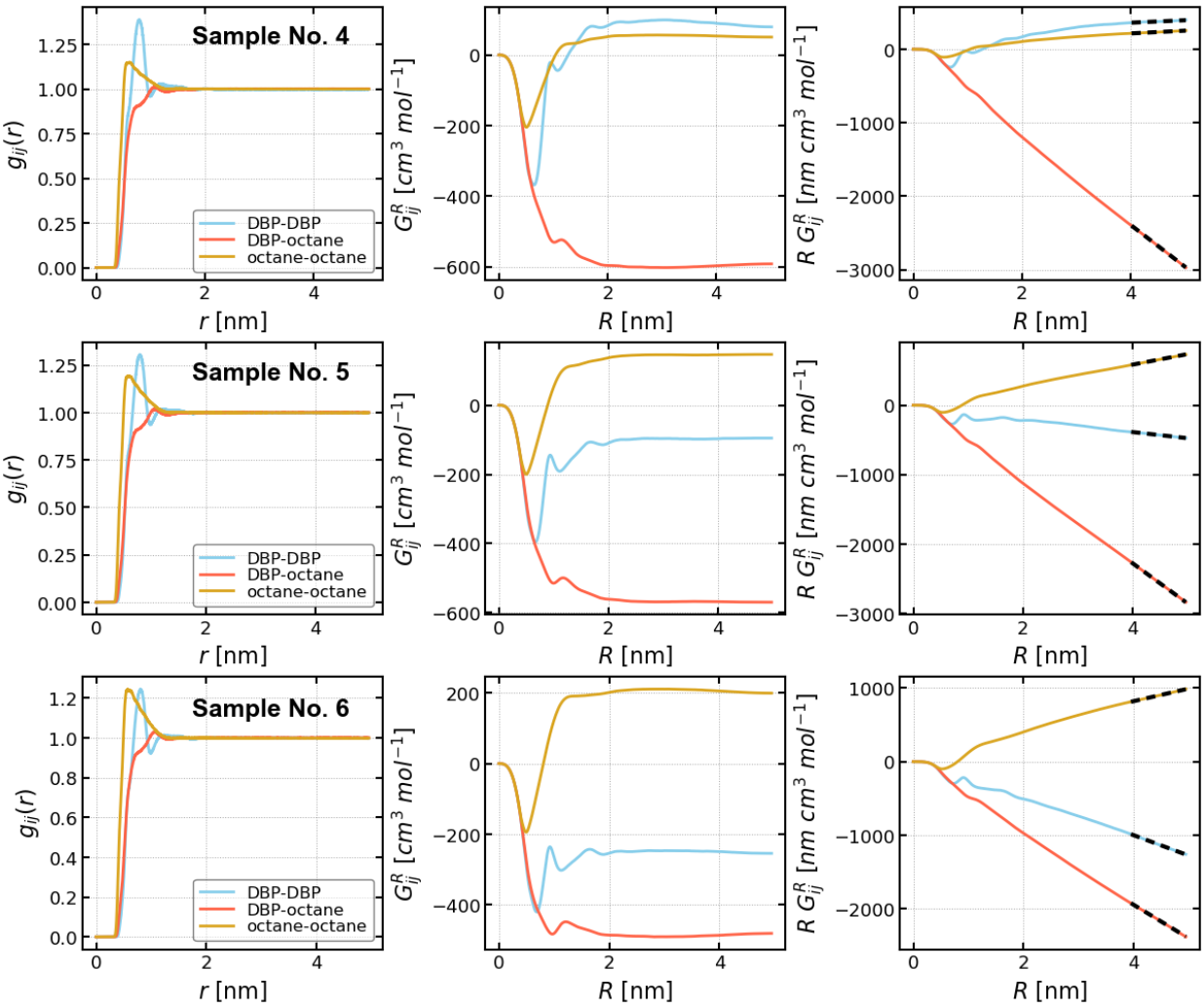

Figure S8: RDF and KBI corrections for DBP/n-octane system, sample no. 4-6.

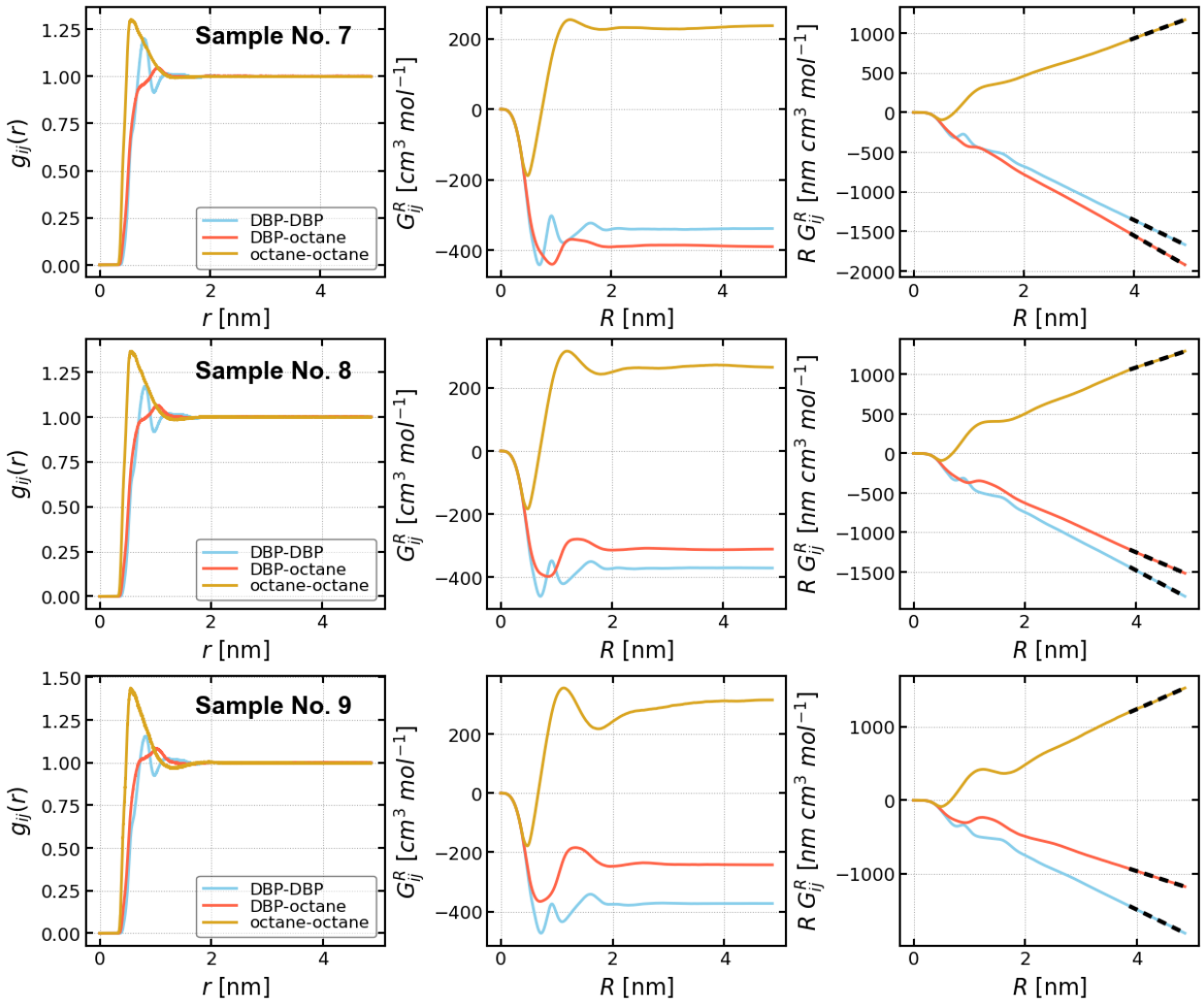

Figure S9: RDF and KBI corrections for DBP/n-octane system, sample no. 7-9.

DBP/*n*-hexane

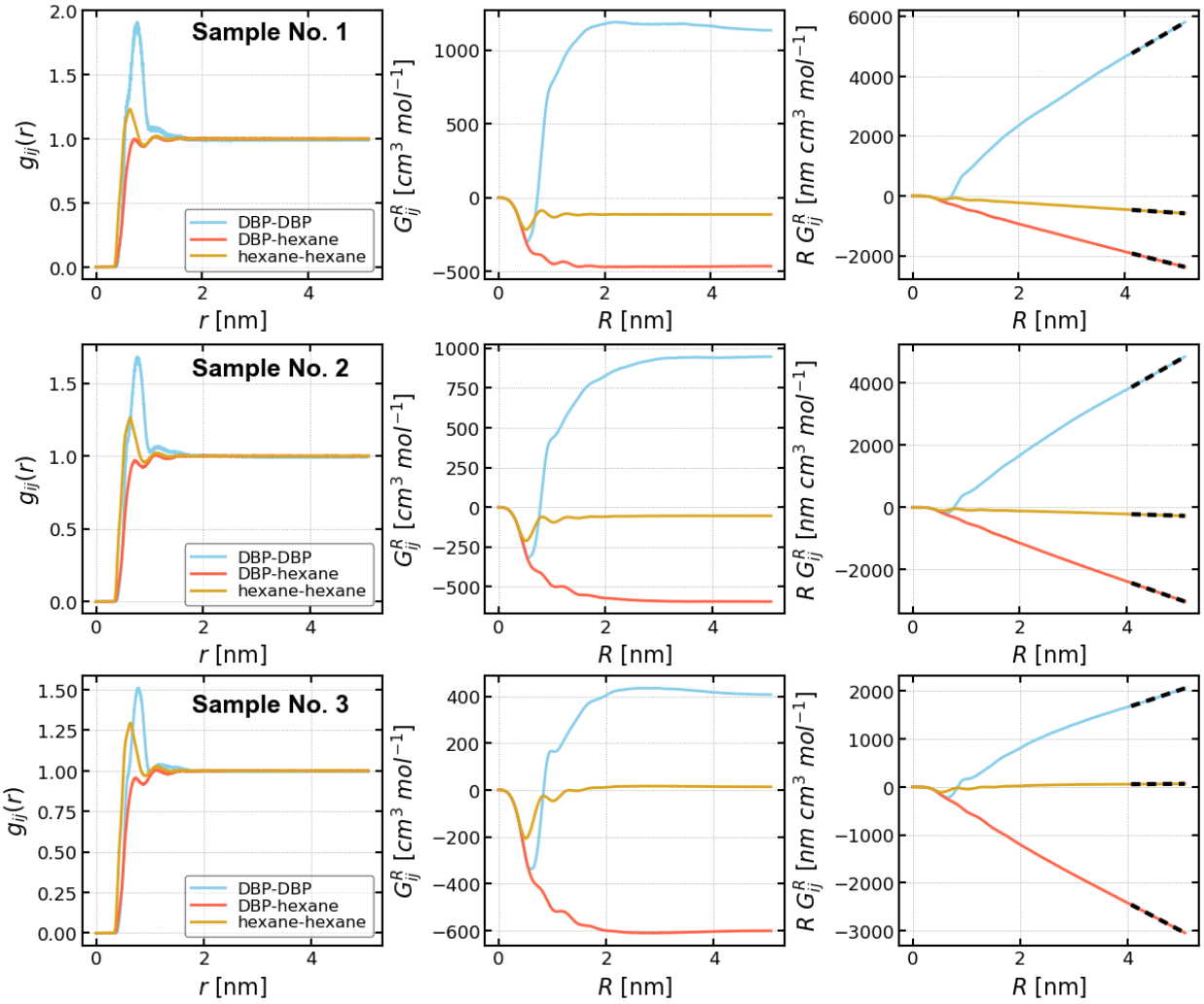

Figure S10: RDF and KBI corrections for DBP/*n*-hexane system, sample no. 1-3.

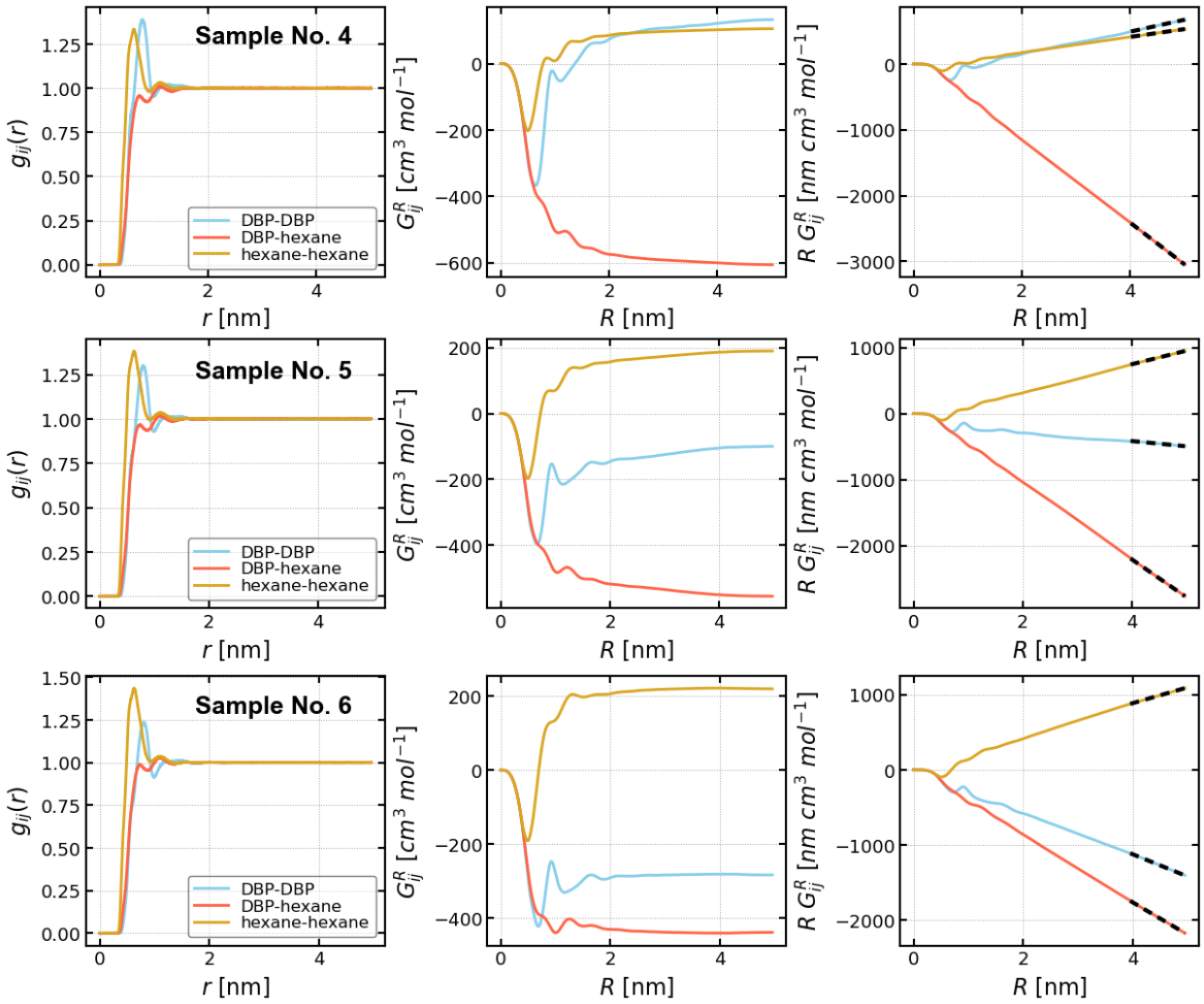

Figure S11: RDF and KBI corrections for DBP/n-hexane system, sample no. 4-6.

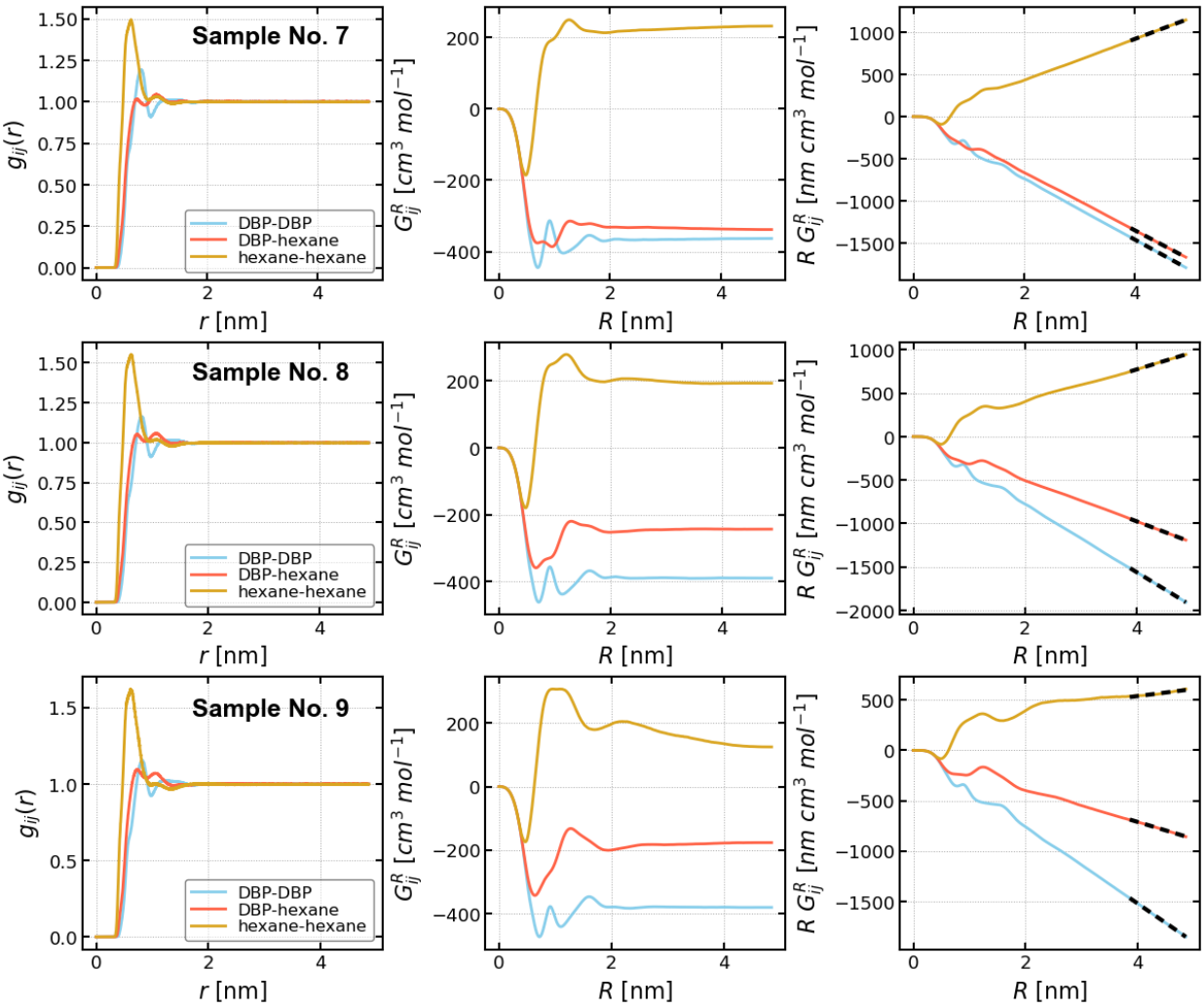

Figure S12: RDF and KBI corrections for DBP/n-hexane system, sample no. 7-9.

DOHE/*n*-dodecane

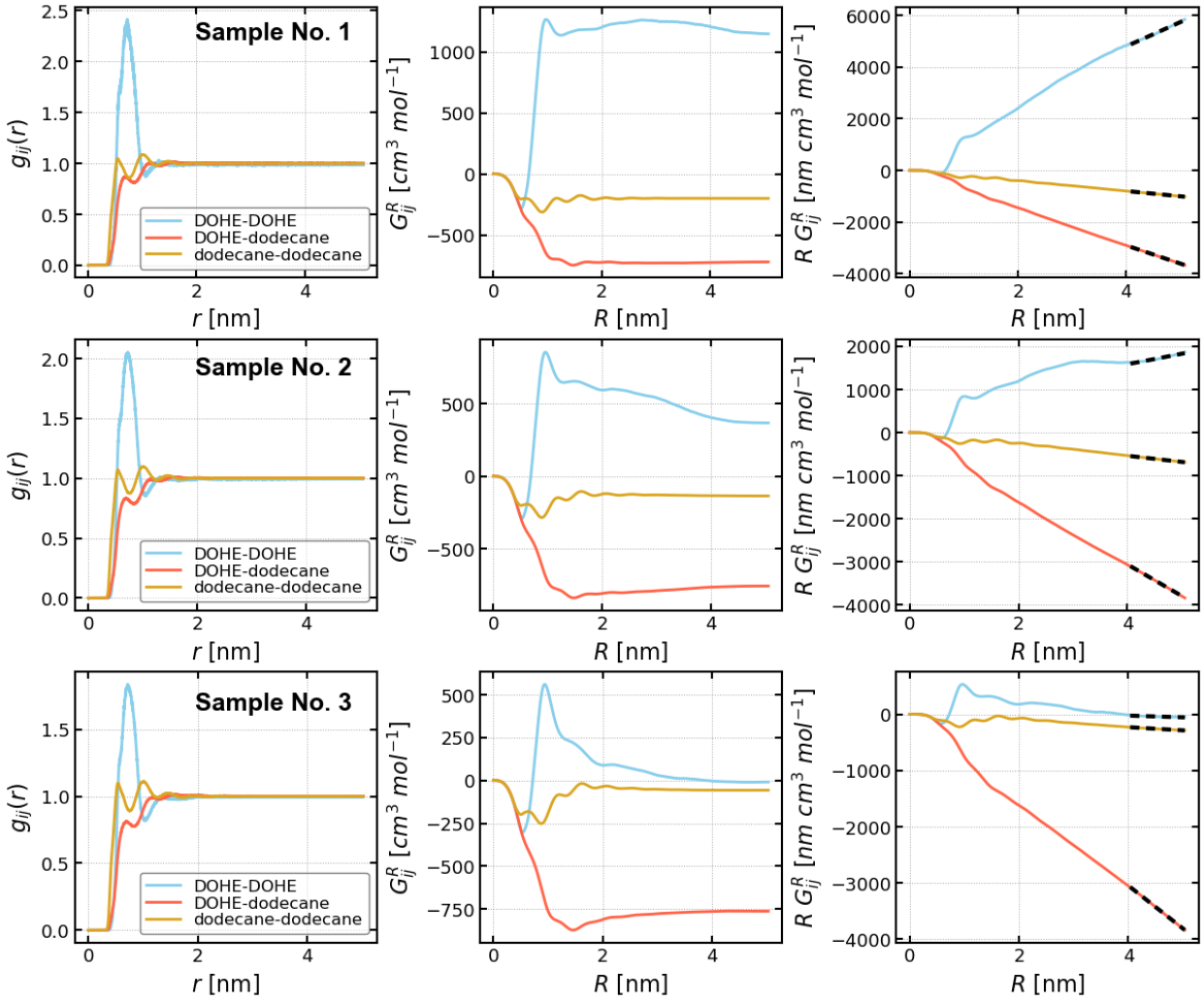

Figure S13: RDF and KBI corrections for DOHE/*n*-dodecane system, sample no. 1-3.

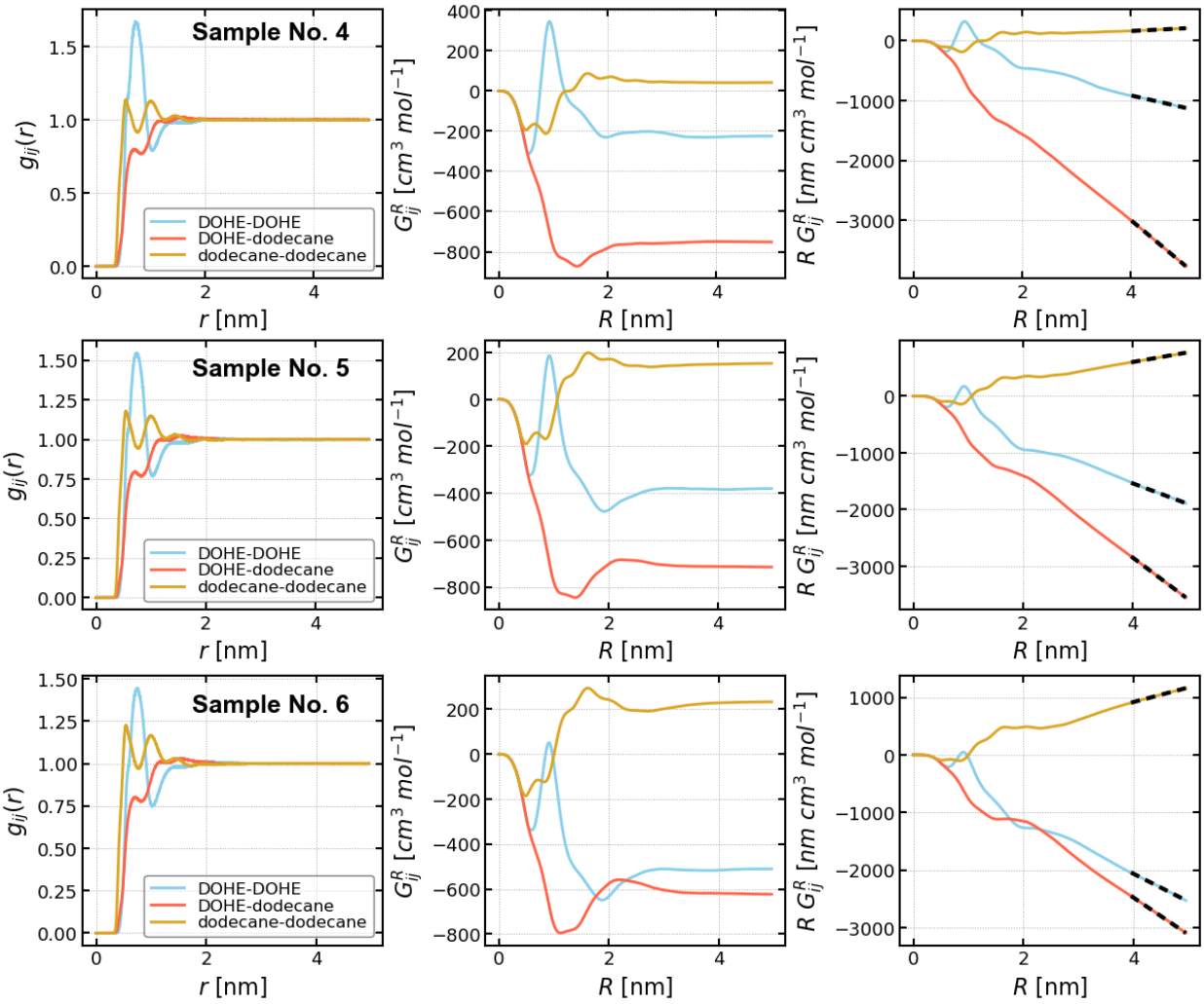

Figure S14: RDF and KBI corrections for DOHE/n-dodecane system, sample no. 4-6.

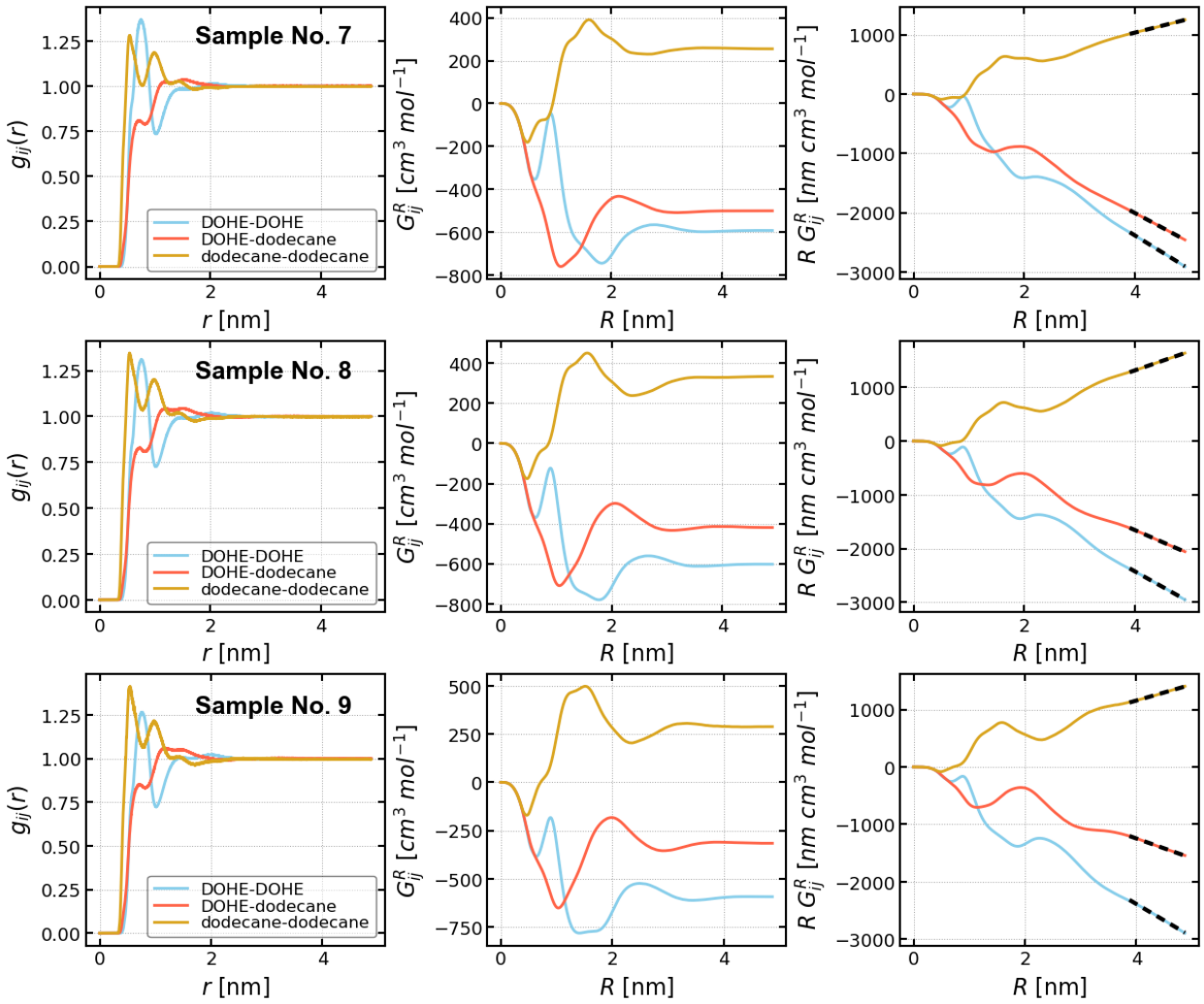

Figure S15: RDF and KBI corrections for DOHE/n-dodecane system, sample no. 7-9.

DOHE/*n*-heptane

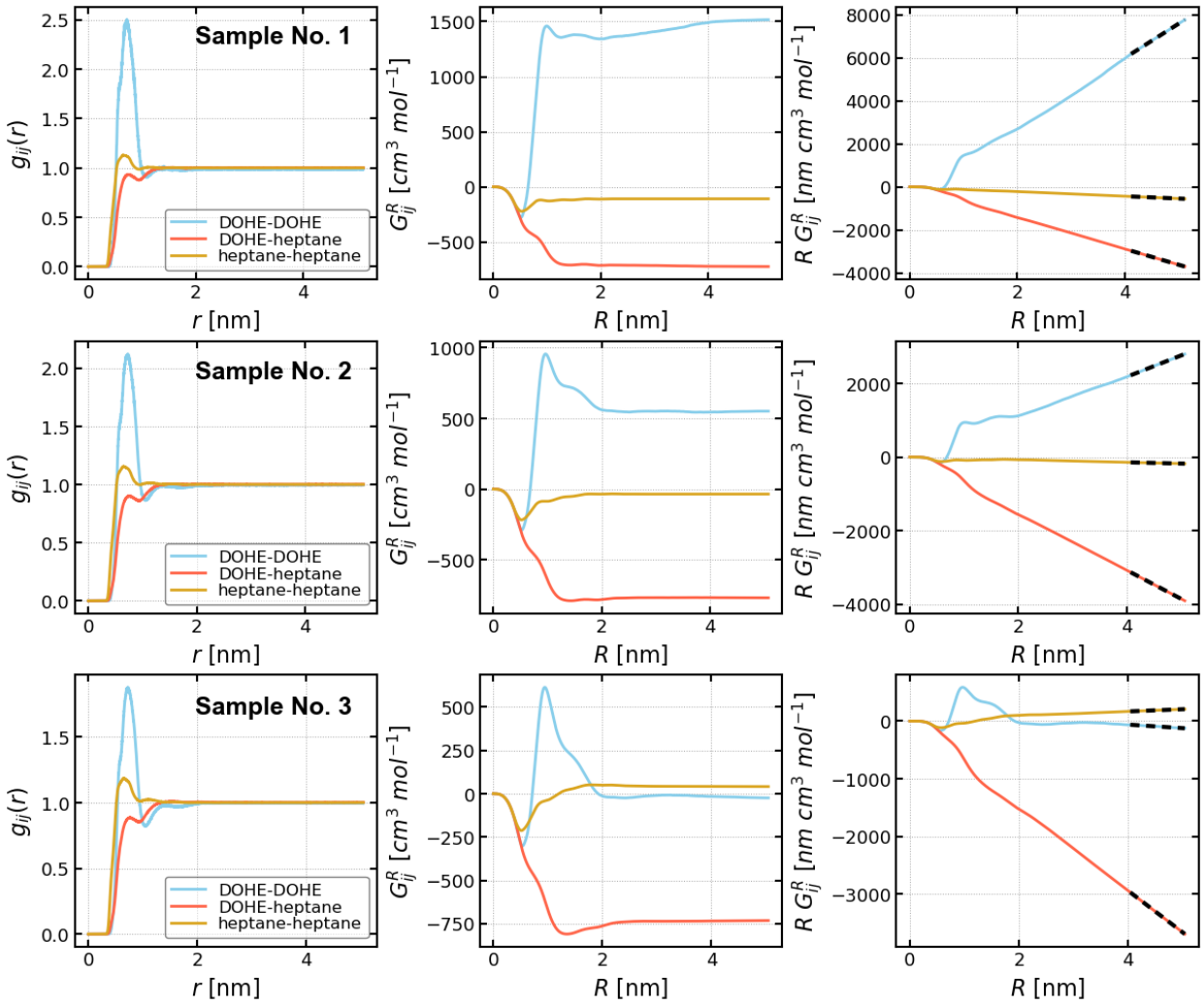

Figure S16: RDF and KBI corrections for DOHE/*n*-heptane system, sample no. 1-3.

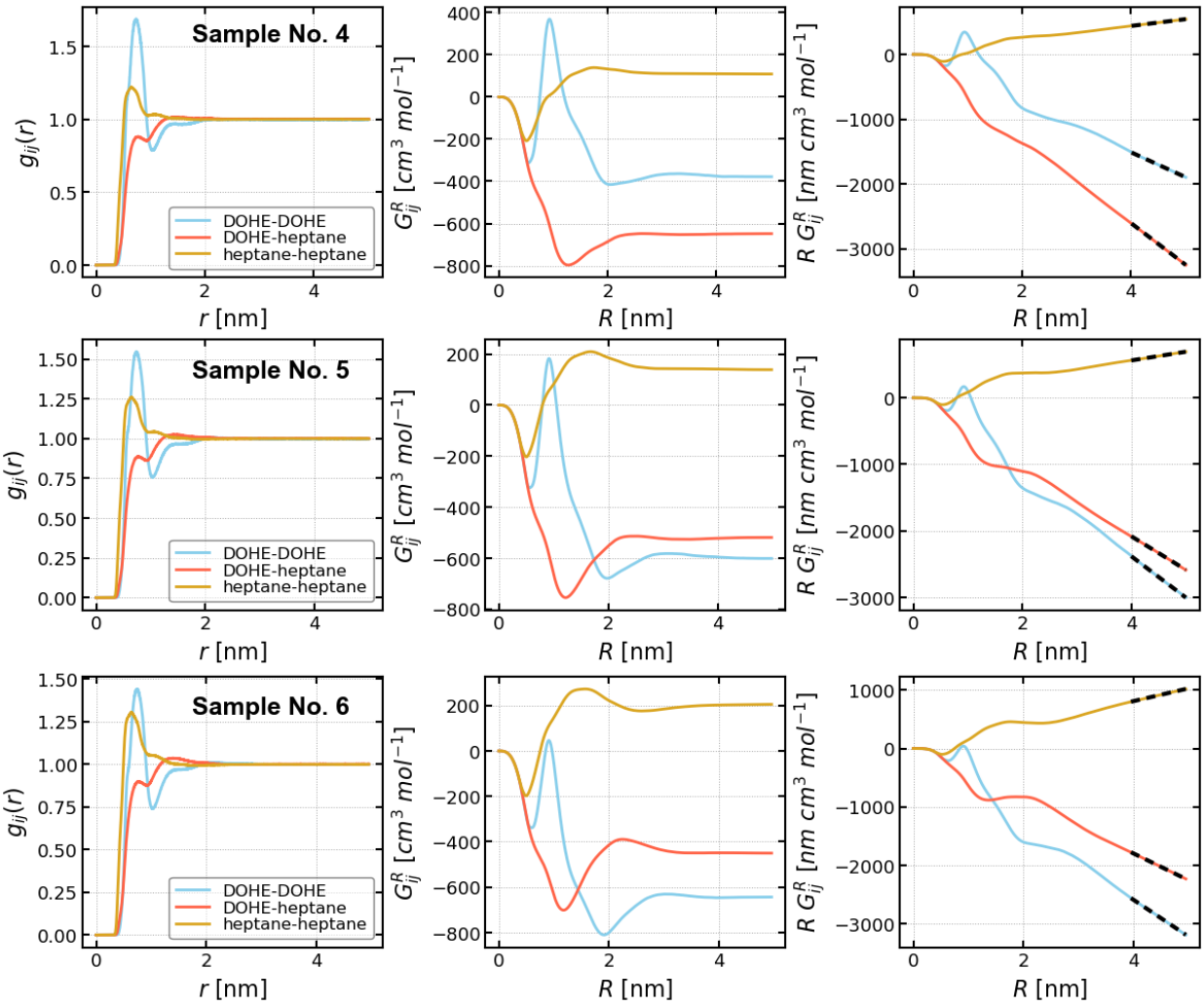

Figure S17: RDF and KBI corrections for DOHE/n-heptane system, sample no. 4-6.

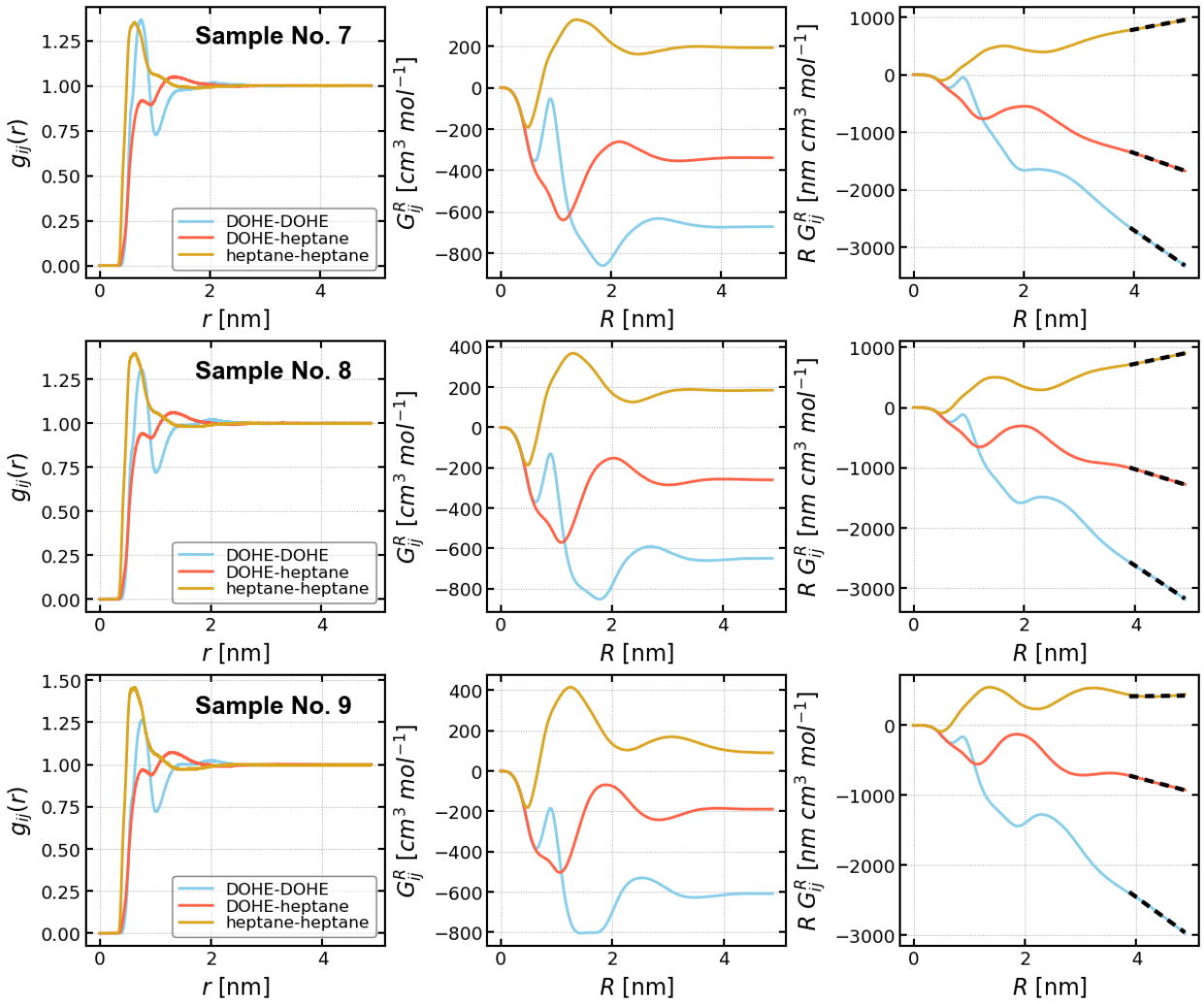

Figure S18: RDF and KBI corrections for DOHE/n-heptane system, sample no. 7-9.

Thermodynamic Models

UNIQUAC

The UNIQUAC (Universal Quasi-Chemical) thermodynamic model[6] employs a local-composition framework with interaction parameters $\tau_{ji} = \exp\left(-\Delta u_{ji}/RT\right)$ to model the enthalpy of mixing,

$$\frac{\Delta H_{mix}}{RT} = -\sum_{i}^{N}\left(x_i q_i \ln \sum_{j}^{N} \theta_j \tau_{ji}\right). \tag{S5}$$

The diagonal elements of Δu_{ij} are zero, giving two interaction parameters for a binary system. Additionally, UNIQUAC uses surface area (q_i) and volume (r_i) parameters to characterize the excess entropy via

$$\frac{S^E}{R} = -\sum_{i}^{N} x_i \ln \frac{\phi_i}{x_i} + \frac{z_c}{2} x_i q_i \ln \frac{\theta_i}{\phi_i}. \tag{S6}$$

Here the surface area term is defined as $\theta_i = x_i q_i / \sum_{j=1}^{N} x_j q_j$, and the volume term is $\phi_i = x_i r_i / \sum_{j}^{N} x_j r_j$. To obtain parameter values for UNIQUAC, interaction parameters were fit to simulated ΔH_{mix} data, while the r_i and q_i parameters are estimated based on the UNIFAC group contributions, since the combinatorial term is identical in both models.[7]

UNIFAC

The UNIFAC model extends the principles of the UNIQUAC model by focusing on subgroup interactions rather than whole molecules, making it a powerful predictive tool for estimating thermodynamic properties in mixtures, as outlined by Fredenslund et al..[8] While it shares the same entropic formulation with UNIQUAC, UNIFAC introduces a distinct enthalpic term that specifically accounts for these subgroup interactions. The enthalpic contribution

in UNIFAC is expressed as

$$\frac{\Delta H_{mix}}{RT} = \sum_{i}^{N} \sum_{k}^{M} x_i \nu_{ki} \left(\ln \Gamma_k - \ln \Gamma_{ki} \right), \tag{S7}$$

where ν_{ki} is the occurrence of subgroup k within molecule i, Γ_k represents the residual activity coefficient of subgroup k within the entire mixture, calculated as

$$\Gamma_k = Q_k \left(1 - \ln \sum_{i}^{N} \Theta_i \psi_{ik} - \sum_{i}^{N} \frac{\Theta_i \psi_{ki}}{\sum_{j}^{N} \Theta_j \psi_{ji}} \right). \tag{S8}$$

Here ψ_{ki} is the residual activity coefficient of subgroup k in a reference solution of pure component i, Θ_i is the surface area term for Q_k in molecule i, and Q_k is the characteristic UNIFAC q parameter for subgroup k.

Pure Component Molar Volumes

Table S8 gives the molar volumes for pure components determined from simulations at 400 K and 300 K and compared to experimental values at 298 K. We report molar volumes from molecular dynamic simulations at 300 K and 400 K for each pure component, with exception of n-dodecane, which we find for GAFF2, as with several common force fields, freezes at unphysically high temperature.[9–11]

Table S8: Comparison of pure component molar volumes (in cm^3 $mole^{-1}$) to experimental values.

Component	V_i^{MD}, 400 K	V_i^{MD}, 300 K	V_i^{exp}, 298 K
DOHE	563	521	521[12]
DBP	359	332	334[13]
n-hexane	152	128	131[14]
n-heptane	167	144	147[14]
n-octane	183	161	163[14]
n-decane	216	192	195[14]
n-dodecane	250	-	228[14]

Negligible Excess Molar Volume

We can obtain the molar volume as a function of composition directly from the MD simulations. If the partial molar volumes are constant, equal to the molar volumes of the pure components, then the excess molar volume will be zero. In Figure S19, the data points show the molar volumes obtained from MD simulations of all systems studied. The straight line is the ideal molar volume calculated from $\overline{V} = xV_1 + (1-x)V_2$, where the V_i are the pure component molar volumes. The good agreement indicates that the excess molar volume is negligible, and we can consider the partial molar volumes to be constant.

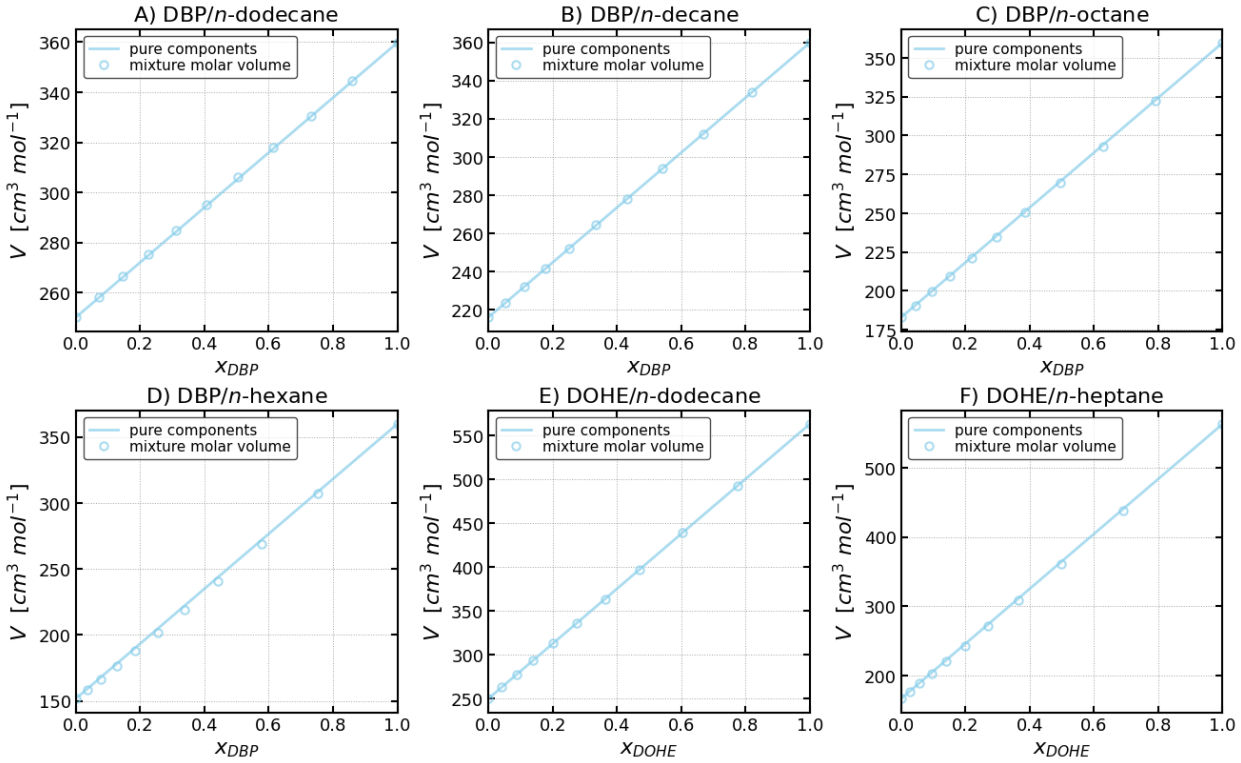

Figure S19: Molar volumes as a function of composition (points) compared with the ideal molar volumes (lines) for all systems studied.

Validation of KBIs from $V_i/\overline{V}$ and κ

In addition to the relation of the KBIs to the mixing free energy curvature given in the main paper, the KBIs are also related to the ratios of the partial and total molar volumes $V_i/\overline{V}$

and to the isothermal compressibility κ. The relations are given by[15]

$$\frac{V_1}{\overline{V}} = \frac{1 + (1-x)\,\rho\,(G_{22}^{\infty} - G_{12}^{\infty})}{1 + x\,(1-x)\,\rho\,(G_{11}^{\infty} + G_{22}^{\infty} - 2G_{12}^{\infty})}, \tag{S9}$$

$$\frac{V_2}{\overline{V}} = \frac{1 + x\,\rho\,(G_{11}^{\infty} - G_{12}^{\infty})}{1 + x\,(1-x)\,\rho\,(G_{11}^{\infty} + G_{22}^{\infty} - 2G_{12}^{\infty})}, \tag{S10}$$

$$\frac{R\,T\,\kappa}{\overline{V}} = \frac{1 + x\,\rho\,G_{11}^{\infty} + (1-x)\,\rho\,G_{22}^{\infty} + x\,(1-x)\,\rho^2\left[G_{11}^{\infty}\,G_{22}^{\infty} - (G_{12}^{\infty})^2\right]}{1 + x\,(1-x)\,\rho\,(G_{11}^{\infty} + G_{22}^{\infty} - 2G_{12}^{\infty})}, \tag{S11}$$

where a typographical error in the original paper has been corrected in Eqn S11. Since these quantities can be independently calculated from the MD simulations, a comparison provides checks on the values of the KBIs obtained by the correction procedure we employ.

Figure S20 compares the ratios $V_i/\overline{V}$ obtained from the KBIs (data points) to those obtained directly from the MD simulations (curves). For the latter, we use the actual MD molar volumes at each composition in the denominator, and the pure component molar volumes in the numerator. The good agreement gives an indication of the accuracy of the KBIs.

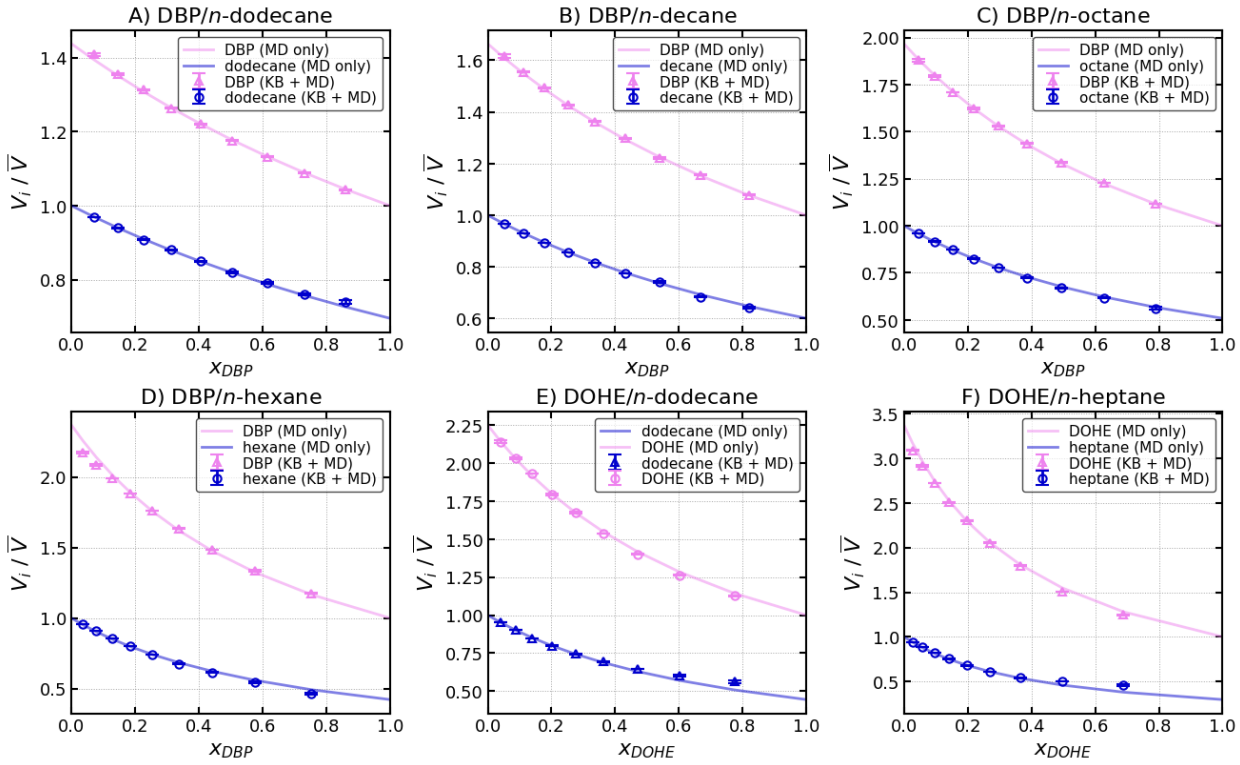

Figure S20: Ratio of partial molar volumes of each component to the total molar volumes for all systems studied. Points are calculated from KBIs, curves are obtained directly from the MD simulations.

Figure S21 compares the isothermal compressibility κ obtained from the KBIs to those obtained directly from the variance of the simulation box volume during the NpT trajectory.[16] While the relative values vary by a factor of two to three, the difference in absolute values are very small, since the compressibilities are negligible for a condensed liquid, especially when the compressibility contribution to the scattering is compared to that of the concentration fluctuations. The small differences between large quantities reflect the relatively small errors in the KBIs.

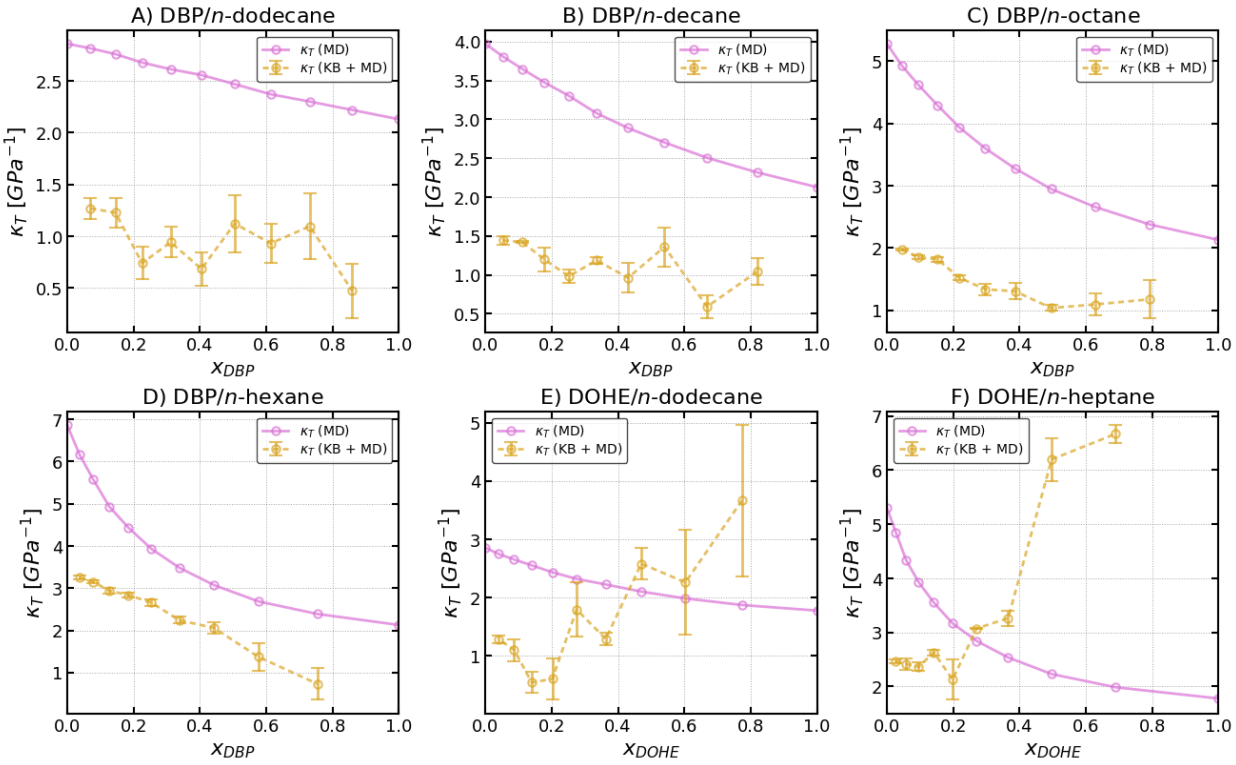

Figure S21: Isothermal compressibilities for all systems studied, obtained from KBIs and directly from the MD simulations.

Error Estimates for Derived Quantities

To obtain the uncertainties in the individual data points for $\partial^2 G^E/\partial x^2$ at $T_{sim} = 400$ K shown in Figure 3 of the main paper, we use conventional propagation of errors from the standard deviations of the G_{ij}^{∞} for that system and composition, which are related to $\partial^2 G^E/\partial x^2$ by Eqns 3 and 4. Likewise the uncertainties in the individual $V_i/\overline{V}$, κ, and I_0 points in Figures S20 -S22 are obtained from the standard deviations of the G_{ij}^{∞} using Eqns S9 - S28 and conventional error propagation.

To obtain the uncertainties in the fit curves for $\partial^2 G^E/\partial x^2$ at $T = 400$ K shown in Figure 3, we use the covariance matrix for the fit parameters obtained from the weighted fit of Eqn. 6. The fit can be obtained analytically using polynomial regression by weighted least

squares.[17] The polynomial can be written as

$$y(x) = \sum_{j=1}^{m} p_j \, x^{j-1}, \tag{S12}$$

where the p_j are the m coefficients of the polynomial of degree $m-1$. In our case, $y = \partial^2 G^E/\partial x^2$, $m = 3$, and the vector of coefficients $\underline{p}$ has components

$$p_1 = 2a_{11} \qquad p_2 = 6a_{111} \qquad p_3 = 12a_{1111}. \tag{S13}$$

We assume we have n data points y_i with uncorrelated errors σ_i at compositions x_i. We wish to minimize the chi-square statistic

$$\chi^2 \equiv \sum_{i=1}^{n} \frac{[y(x_i) - y_i]^2}{\sigma_i^2}. \tag{S14}$$

This can be done analytically by setting each of its partial derivatives w.r.t. the p_j to zero,

$$0 = \frac{\partial \chi^2}{\partial p_j} = \sum_{i=1}^{n} \frac{2\left[\sum_{k=1}^{m} p_k \, x_i^{k-1} \; - y_i\right] x_i^{j-1}}{\sigma_i^2} \tag{S15}$$

for $j = 1$ to m. These equations can be written as the matrix equation

$$0 = \mathbf{M}\,\underline{p} - \underline{v}, \tag{S16}$$

where in the last line we have defined the $m \times m$ matrix $\mathbf{M}$ with components

$$M_{jk} \equiv \sum_{i=1}^{n} \frac{x_i^{j-1} \, x_i^{k-1}}{\sigma_i^2} \tag{S17}$$

and the $m \times 1$ vector $\underline{v}$ with components

$$v_j \equiv \sum_{i=1}^{n} \frac{x_i^{j-1} \, y_i}{\sigma_i^2}. \tag{S18}$$

The solution for the parameters that minimize chi-square can thus be obtained from

$$\underline{p} = \mathbf{M^{-1}}\,\underline{v}, \tag{S19}$$

where $\mathbf{M^{-1}}$ is the inverse of the matrix $\mathbf{M}$. The variance-covariance matrix of the fit parameters is given by

$$\mathbf{C} = \frac{\chi^2}{n-m}\,\mathbf{M^{-1}}. \tag{S20}$$

The uncertainty in the fit function $y = \partial^2 G^E/\partial x^2$ is then given by

$$\sigma_y(x) = \left[\sum_{j=1}^{m}\sum_{k=1}^{m} C_{jk}\,x^{j-1}\,x^{k-1}\right]^{1/2}. \tag{S21}$$

These give the 68% confidence bands $y(x) \pm \sigma_y(x)$ shown in Figure 3 where $y(x)$ is evaluated using the best-fit parameters determined by Eqn S19.

From these confidence bands, we can obtain those for $I_0(x)$ and $T_{sp}(x)$ shown in Figure 6. We first extrapolate the free energy curvature at the simulation temperature T_{sim} to any other temperature T under the assumption of temperature-independent ΔH_{mix} and ΔS_{mix} using

$$\begin{aligned}\frac{\partial^2 \Delta G_{mix}(x,T)}{\partial x^2} &= \frac{\partial^2 \Delta H_{mix}(x)}{\partial x^2} - T\,\frac{\partial^2 \Delta S_{mix}(x)}{\partial x^2} \\ &= \frac{\partial^2 \Delta H_{mix}(x)}{\partial x^2} + \frac{T}{T_{sim}}\left(\frac{\partial^2 \Delta G_{mix}(x,T_{sim})}{\partial x^2} - \frac{\partial^2 \Delta H_{mix}(x)}{\partial x^2}\right).\end{aligned} \tag{S22}$$

From this, one can see that the uncertainty in $\partial^2 \Delta G_{mix}/\partial x^2$ scales simply with T according to

$$\sigma_y(x,T) = \frac{T}{T_{sim}}\,\sigma_y(x,T_{sim}) \tag{S23}$$

if we negelect any uncertainty in $\partial^2 \Delta H_{mix}/\partial x^2$. Since I_0 is inversely related to $\partial^2 \Delta G_{mix}/\partial x^2$

according to Eqn 10, its uncertainty can be expressed as

$$\frac{\sigma_{I_0}(x,T)}{I_0(x,T)} = \frac{\sigma_y(x,T)}{\frac{\partial^2 \Delta G_{mix}(x,T)}{\partial x^2}} = \frac{\sigma_y(x,T_{sim})}{\frac{\partial^2 \Delta G_{mix}(x,T_{sim})}{\partial x^2} + \frac{\partial^2 \Delta H_{mix}(x)}{\partial x^2}\,\frac{T_{sim}-T}{T}} \tag{S24}$$

The spinodal temperature T_{sp} is the temperature where $\partial^2 \Delta G_{mix}/\partial x^2$ becomes zero. From Eqn S22, we obtain

$$T_{sp} = \frac{-T_{sim}\,\frac{\partial^2 \Delta H_{mix}(x)}{\partial x^2}}{\frac{\partial^2 \Delta G_{mix}(x,T_{sim})}{\partial x^2} - \frac{\partial^2 \Delta H_{mix}(x)}{\partial x^2}}. \tag{S25}$$

Thus the uncertainty in T_{sp} is given by

$$\frac{\sigma_{T_{sp}}}{T_{sp}} = \frac{\sigma_y(x,T_{sim})}{\frac{\partial^2 \Delta G_{mix}(x,T_{sim})}{\partial x^2} - \frac{\partial^2 \Delta H_{mix}(x)}{\partial x^2}}. \tag{S26}$$

Contribution of Vibrational Term to Scattering

For a binary system, the x-ray scattering cross section per unit volume as $q \to 0$ can be written as the sum of two terms: I_0^x from composition fluctuations, and I_0^ρ from vibrations,[18]

$$I_0 = \frac{r_e^2\, N_A}{\rho}\left(\frac{\partial \rho^e}{\partial x}\right)^2 RT\,\left(\frac{\partial^2 \Delta G_{mix}}{\partial x^2}\right)^{-1} + r_e^2\, N_A\, \rho\, \overline{Z}^2\, \frac{R\,T\,\kappa}{\overline{V}}, \tag{S27}$$

$$\frac{\partial \rho^e}{\partial x} = \rho\left(\frac{Z_1 V_2 - Z_2 V_1}{\overline{V}}\right), \tag{S28}$$

where $r_e^2 = 7.95\times10^{-26}$ cm^2/electron is the electron scattering cross section, $N_A = 6.02\times10^{23}$ electrons/mole is Avogadro's number, $\rho^e = \rho\,[x\,Z_1 + (1-x)\,Z_2]$ is the molar electron density, Z_i is the number of electrons per molecule, $\overline{Z} = x\,Z_1 + (1-x)\,Z_2$ is the average number of electrons per molecule, V_i is the partial molar volume of component i, $\overline{V} = x\,V_1 + (1-x)\,V_2 = 1/\rho$ is the molar volume of the solution, and κ is the isothermal compressibility from MDKB→Phase. To obtain Eqn S28, we assume that the partial molar volumes are independent of composition and equal to the molar volumes of the pure components, so

that the excess molar volume is negligible. Above, we demonstrate that this is a good approximation for our systems. We use the experimental pure component V_i at 295 K and the ideal formula for $\overline{V}$ in calculating the x-ray scattering intensities.

Figure S22 illustrates the relative size of the two terms in I_0. Here, we use the values of $\partial^2 \Delta G_{mix}/\partial x^2$ and κ at the temperature of the simulation, $T = T_{sim} = 400$ K, which gives a smaller contribution from composition fluctuations than at the experimental temperature $T = 295$ K. Even so, the term from vibrations is always negligible, so we neglect it in the expression used in the main paper.

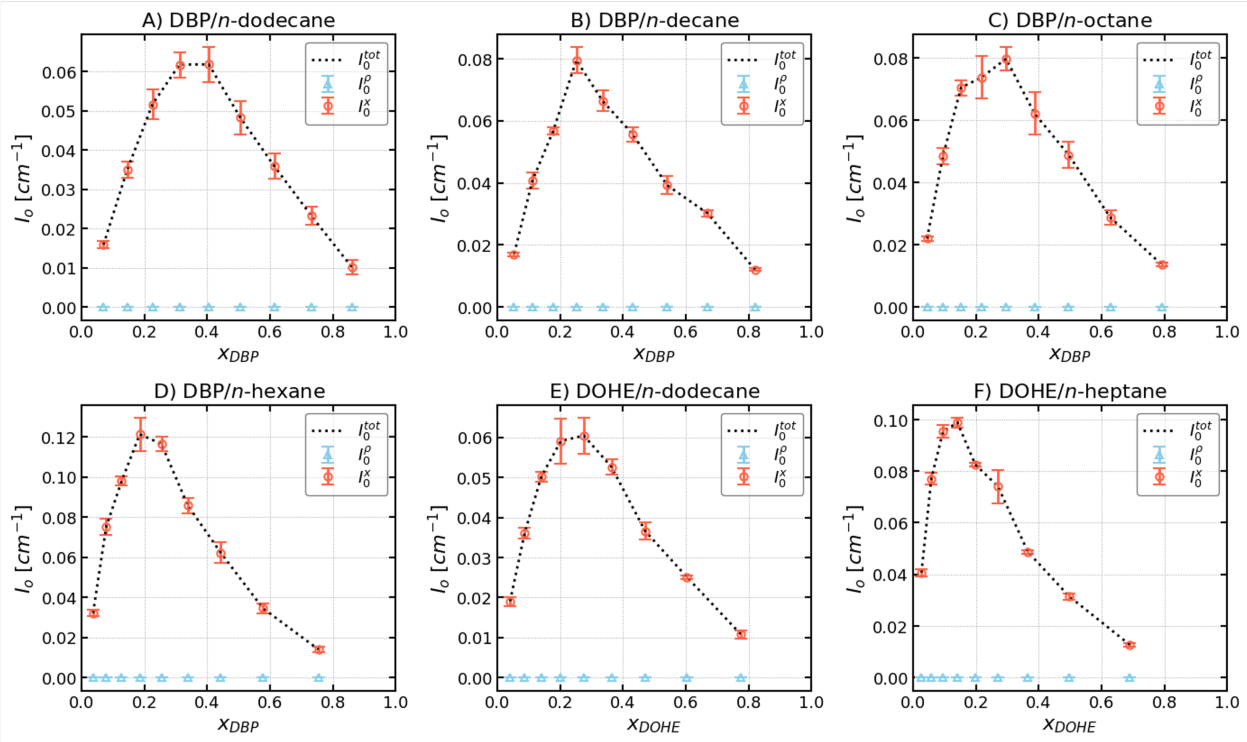

Figure S22: Breakdown of contributions to I_0 at $T = 400$ K from isothermal compressibility term (vibrations) compared to the concentration fluctuation term in all systems studied, showing that compressibility term is negligible.

Calculated Enthalpy and Entropy and Comparison to Thermodynamic Models

As described in the main text, enthalpy of mixing values were obtained directly from the MD simulations and fit to a polynomial. From these, curves for the entropy of mixing were obtained. The results from the MDKB→Phase approach were compared with those from established thermodynamic models—UNIQUAC, UNIFAC, and COSMO-RS. Typical results for DBP/n-dodecane are presented in the main paper; results for other systems are given here. Similar to observations made with the DBP/n-dodecane system, the enthalpic and entropic contributions estimated by these traditional models tend to be underestimated for the remaining systems. This underestimation leads to more pronounced deviations in ΔG_{mix} compared to those obtained using the MDKB→Phase approach.

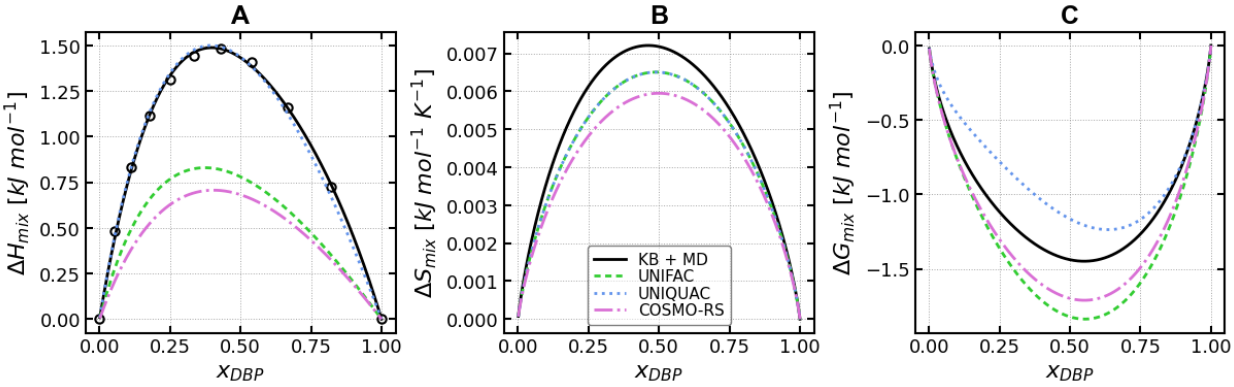

Figure S23: Comparison of enthalpic and entropic contributions from various thermodynamic models for DBP in n-decane.

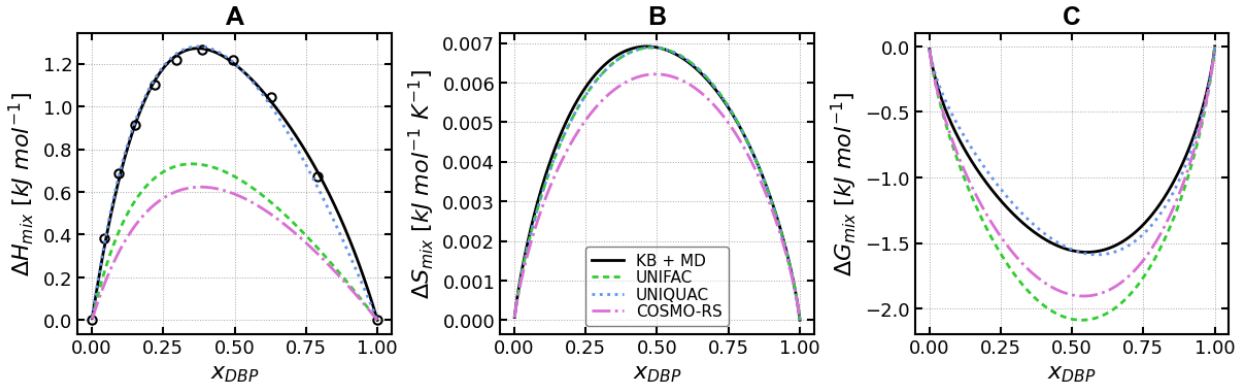

Figure S24: Comparison of enthalpic and entropic contributions from various thermodynamic models for DBP in n-octane.

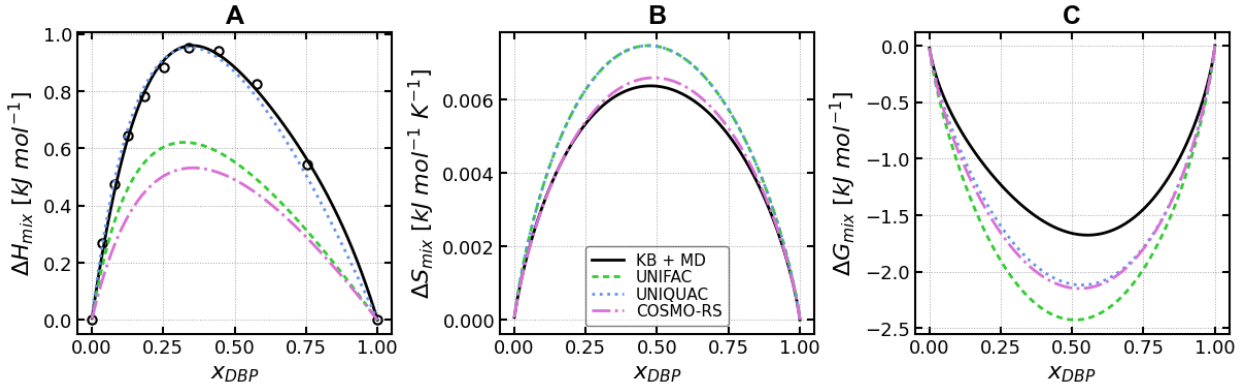

Figure S25: Comparison of enthalpic and entropic contributions from various thermodynamic models for DBP in n-hexane.

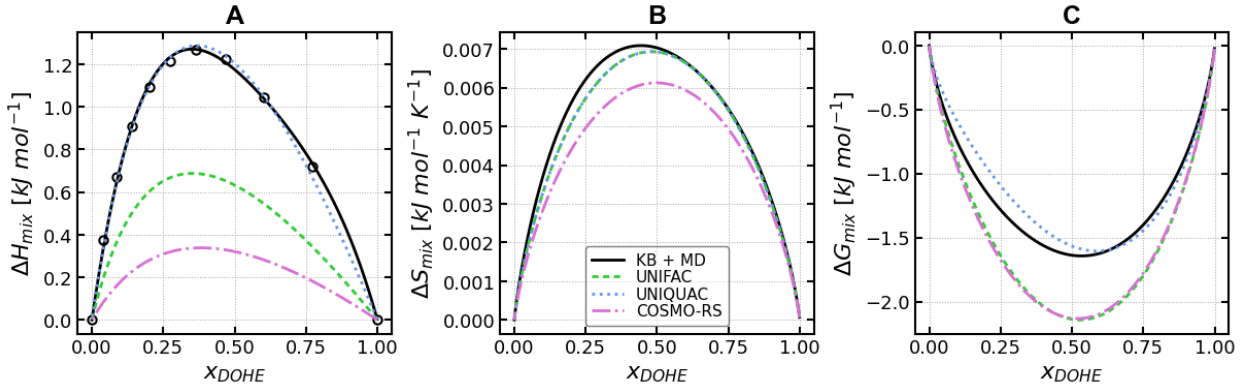

Figure S26: Comparison of enthalpic and entropic contributions from various thermodynamic models for DOHE in n-dodecane.

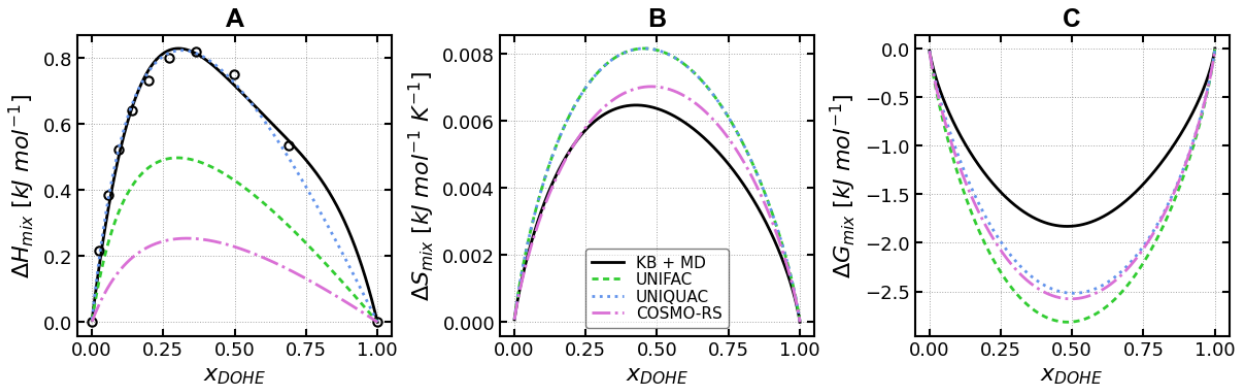

Figure S27: Comparison of enthalpic and entropic contributions from various thermodynamic models for DOHE in n-heptane.

Temperature Independence of ΔH_{mix} and ΔS_{mix}

To verify that both ΔH_{mix} and ΔS_{mix} are independent of temperature, DBP/n-dodecane was selected as a case study, with MD simulations conducted at temperatures of 380 K, 400 K, and 410 K. We calculated ΔH_{mix} and ΔS_{mix} from simulations at each T using the MDKB→Phase method. The results, as depicted in Figure S28, confirm that ΔH_{mix} and ΔS_{mix} are essentially independent of T in a typical malonamide-alkane binary system. Establishing this temperature independence allows for the accurate estimation of ΔG_{mix} at any T using values of ΔH_{mix} and ΔS_{mix} obtained from simulations at a different T through the relation $\Delta G_{mix}(T) = \Delta H_{mix} - T\Delta S_{mix}$.

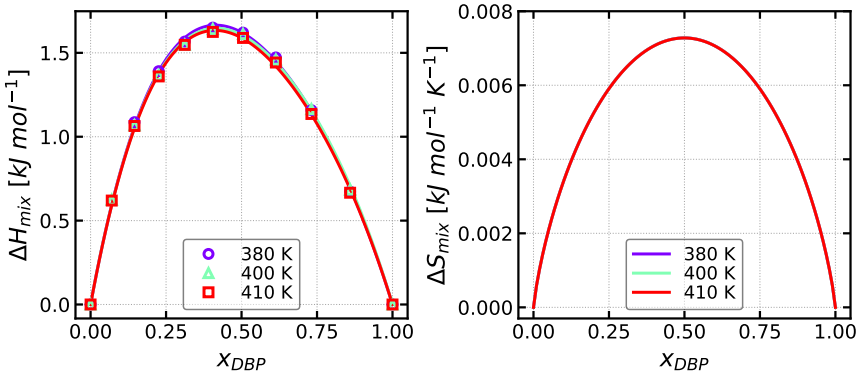

Figure S28: Comparison of ΔH_{mix} and ΔS_{mix} calculated for DBP in n-dodecane from simulations at 380, 400, and 410 K.

Our assumption that ΔH_{mix} and ΔS_{mix} are independent of T is typical for models of solution thermodynamics. The UNIQUAC, UNIFAC, and COSMO-RS models give values for ΔS_{mix} that are independent of T, and the predicted ΔH_{mix} vary only from one to fifteen percent over 100 K for typical parameter values (see Fig. S29). Thus the MDKB→Phase method is consistent with conventional model approaches and should be applicable to a similarly broad range of systems, and likely with a higher accuracy in determining ΔH_{mix} and ΔS_{mix}, as discussed in the main manuscript text. We note that to obtain the T_c values for the UNIQUAC, UNIFAC, and COSMO-RS models shown in Table 1, we used their slightly temperature-dependent values of ΔH_{mix}.

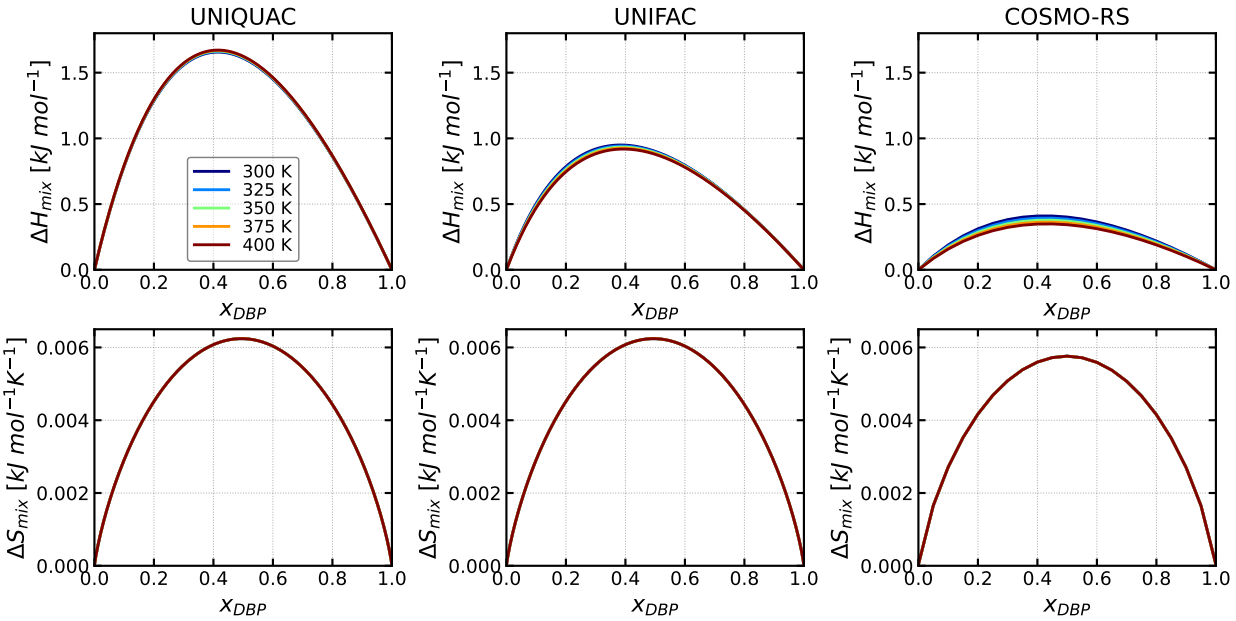

Figure S29: Calculated T dependence of $\Delta H_{mix}(x)$ and $\Delta S_{mix}(x)$ for DBP in n-dodecane, using the UNIQUAC, UNIFAC, and COSMO-RS models with parameters obtained as described in the main text.

Liquid-Liquid Phase Equilibria

Using the results from the MDKB→Phase approach, phase diagrams were computed by estimating ΔG_{mix} as a function of temperature. Results for the DBP/n-dodecane system are shown in the main paper; results for other systems are shown here. In each figure, the left panel depicts ΔG_{mix} at various temperatures with binodal and spinodal points in black closed and open circles, respectively, the center panel is a heatmap of ΔG_{mix} with the solid binodal and dashed spinodal curves overlaid, and the right panel is a heatmap of the calculated SAXS I_0 values at each temperature with the solid binodal and dashed spinodal curves overlaid. The phase diagrams correspond to those compared with experimental SAXS I_0 data in the main text.

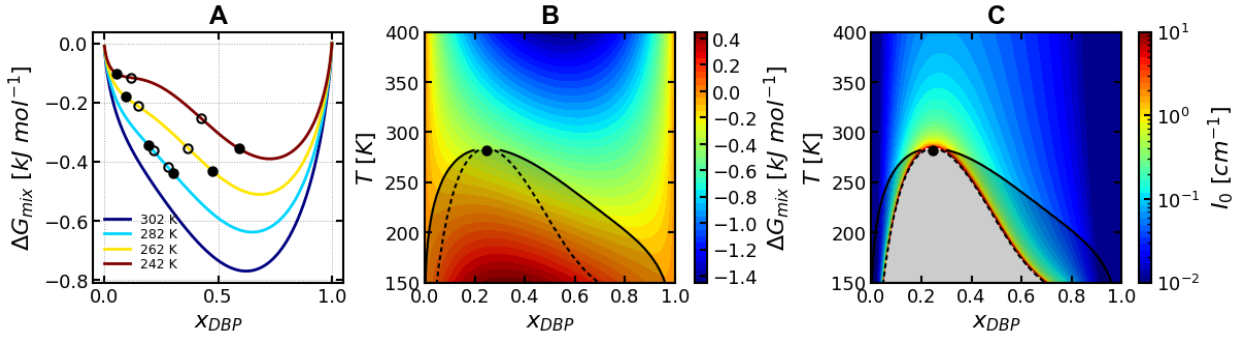

Figure S30: Results for phase equilibria using the MDKB→Phase approach for DBP in n-decane.

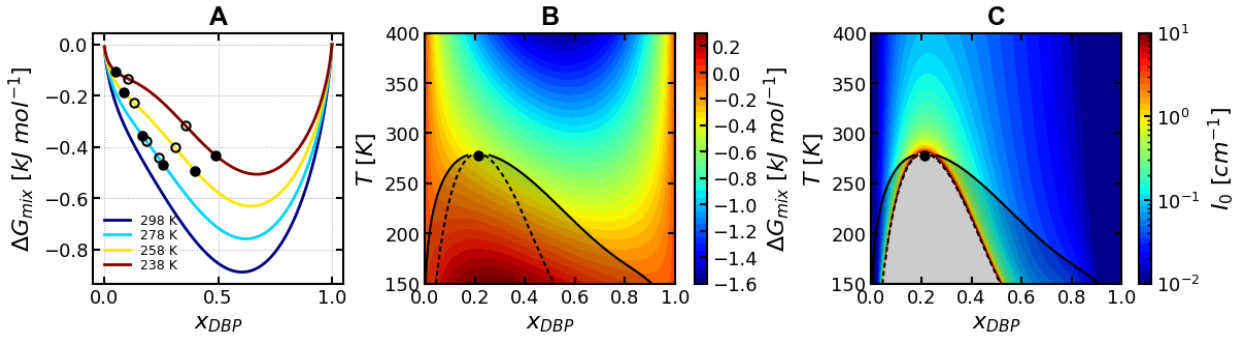

Figure S31: Results for phase equilibria using the MDKB→Phase approach for DBP in n-octane.

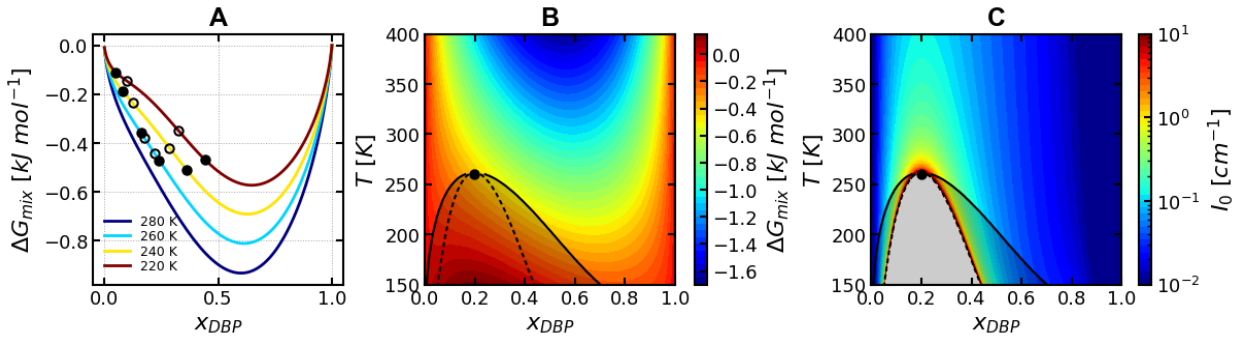

Figure S32: Results for phase equilibria using the MDKB→Phase approach for DBP in *n*-hexane.

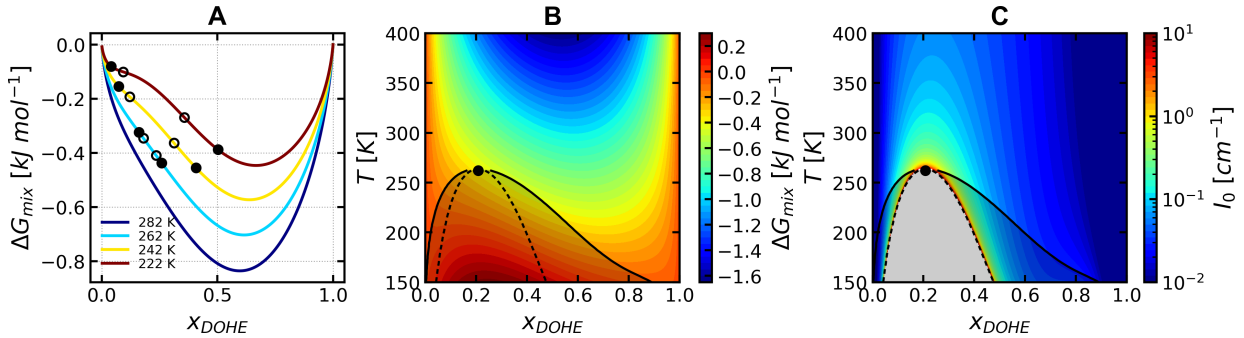

Figure S33: Results for phase equilibria using the MDKB→Phase approach for DOHE in *n*-dodecane.

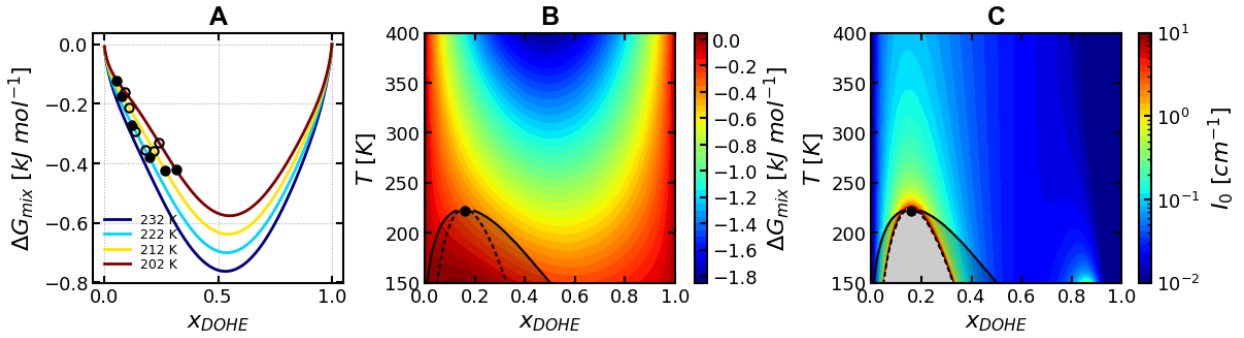

Figure S34: Results for phase equilibria using the MDKB→Phase approach for DOHE in *n*-heptane.

Critical Point Comparisons

Table S9 tabulates the critical temperatures and critical compositions obtained from the MDKB→Phase approach, for each of the six systems studied in this work.

Table S9: Critical temperature and critical extractant mole fraction determined from MDKB→Phase model, with error on the last digit shown in parenthesis

system	T_c (K)	x_c	ϕ_c
DBP/*n*-dodecane	288(1)	0.271	0.354
DBP/*n*-decane	282(3)	0.247	0.359
DBP/*n*-octane	278(4)	0.212	0.357
DBP/*n*-hexane	260(3)	0.200	0.390
DOHE/*n*-dodecane	262(2)	0.208	0.375
DOHE/*n*-heptane	222(5)	0.159	0.402

References

(1) Milzetti, J.; Nayar, D.; van der Vegt, N. F. A. Convergence of Kirkwood–Buff Integrals of Ideal and Nonideal Aqueous Solutions Using Molecular Dynamics Simulations. *J. Phys. Chem. B* **2018**, *122*, 5515–5526.

(2) Ganguly, P.; van der Vegt, N. F. A. Convergence of Sampling Kirkwood–Buff Integrals of Aqueous Solutions with Molecular Dynamics Simulations. *J. Chem. Theory Comput.* **2013**, *9*, 1347–1355.

(3) Krüger, P.; Schnell, S. K.; Bedeaux, D.; Kjelstrup, S.; Vlugt, T. J. H.; Simon, J.-M. Kirkwood–Buff Integrals for Finite Volumes. *J. Phys. Chem. Lett.* **2013**, *4*, 235–238.

(4) Dohn, A. O.; Markmann, V.; Nimmrich, A.; Haldrup, K.; Møller, K. B.; Nielsen, M. M. Eliminating finite-size effects on the calculation of x-ray scattering from molecular dynamics simulations. *J. Chem. Phys.* **2023**, *159*, 124115.

(5) Simon, J.-M.; Krüger, P.; Schnell, S. K.; Vlugt, T. J. H.; Kjelstrup, S.; Bedeaux, D. Kirkwood–Buff integrals: From fluctuations in finite volumes to the thermodynamic limit. *J. Chem. Phys.* **2022**, *157*, 130901.

(6) Abrams, D. S.; Prausnitz, J. M. Statistical Thermodynamics of Liquid Mixtures: A New Expression for the Excess Gibbs Energy of Partly or Completely Miscible Systems. *AIChE J.* **1975**, *21*, 116–128.

(7) Gmehling, J.; Kolbe, B.; Kleiber, M.; Rarey, J. *Chemical Thermodynamics for Process Simulation*; Wiley-VCH, 2012.

(8) Fredenslund, A.; Jones, R.; Prausnitz, J. M. Group-contribution estimation of activity coefficients in nonideal liquid mixtures. *AIChE J.* **1975**, *21*, 1086–1099.

(9) Siu, S. W.; Pluhackova, K.; Bockmann, R. A. Optimization of the OPLS-AA force field for long hydrocarbons. *J. Chem. Theory Comput.* **2012**, *8*, 1459–1470.

(10) Vo, Q. N.; Hawkins, C.; Dang, L. X.; Nilsson, M.; Nguyen, H. D. A Computational Study of Molecular Structure and Self-Association of Tri-n-butyl Phosphates in n-Dodecane Diluent. *J. Phys. Chem. B* **2015**, *119*, 1588–1597.

(11) Servis, M.; Tormey, C.; Wu, D.; Braley, J. A Molecular Dynamics Study of Tributyl Phosphate and Diamyl Amyl Phosphonate Self-Aggregation in Dodecane and Octane. *J. Phys. Chem. B* **2016**, *120*, 2796–2806.

(12) Bonnett, B.; Rahman, T.; Poe, D.; Seifert, S.; Stephenson, G. B.; Servis, M. J. Insights into water extraction and aggregation mechanisms of malonamide-alkane mixtures. *Phys. Chem. Chem. Phys.* **2024**, *26*, 18089–18101.

(13) Bonnett, B. L.; Sheyfer, D.; Wimalasiri, P. N.; Nayak, S.; Lal, J.; Zhang, Q.; Seifert, S.; Stephenson, G. B.; Servis, M. J. Critical fluctuations in liquid–liquid extraction organic phases controlled by extractant and diluent molecular structure. *Phys. Chem. Chem. Phys.* **2023**, *25*, 16389–16403.

(14) Tardajos, G.; na, M. D. P.; Aicart, E. Speed of sound in pure liquids by a pulse-echo-overlap method. *J. Chem. Thermodynamics* **1986**, *18*, 683–689.

(15) Kirkwood, J. G.; Buff, F. P. The Statistical Mechanics Theory of Solutions. I. *J. Chem. Phys.* **1951**, *19*, 774–777.

(16) Ning, F.; Glavatskiy, K.; Ji, Z.; Kjelstrup, S.; Vlugt, T. H. Compressibility, thermal expansion coefficient and heat capacity of CH 4 and CO 2 hydrate mixtures using molecular dynamics simulations. *Phys. Chem. Chem. Phys.* **2015**, *17*, 2869–2883.

(17) Wolberg, J. R. *Data analysis using the method of least squares : extracting the most information from experiments*; Springer-Verlag Berlin Heidelberg, 2006.

(18) Nishikawa, K. The Solution Chemistry of Mixing States Probed via Fluctuations: a

Direct Description of Inhomogeneity in Mixing. *Bull. Chem. Soc. Jpn.* **2021**, *94*, 2170–2186.